

# CRB for a Generic Near-Field Positioning System Using Three Electric Field Types

Ang Chen, Li Chen, *Senior Member, IEEE*, Yunfei Chen, *Senior Member, IEEE*, and Guo Wei

**Abstract**—The use of larger antenna arrays at higher frequency bands is envisioned in the beyond 5G wireless networks. This takes advantage of the near-field propagation regime where the wavefront is no longer plane but spherical, bringing both new opportunities and challenges for the high-precision positioning. In this paper, a generic near-field positioning model with different observation capabilities for three electric fields (*vector, scalar, and overall scalar electric field*) is proposed. For these three electric field types, the Cramér-Rao bound (CRB) is adopted to evaluate the achievable estimation accuracy. The expressions of the CRBs using different electric field observations are derived by combining electromagnetic theory with estimation theory. Closed-form expressions can be further obtained if the terminal is located on the central perpendicular line (CPL) of the receiving antenna surface. In addition, the above discussions are extended to the system with multiple distributed receiving antennas under the CPL assumption. The CRBs using various electric fields in this case are derived and the effect of different numbers of receiving antennas on estimation accuracy is investigated. Numerical results are provided to quantify the CRBs and validate the analytical results. Also, the impact of various system parameters, including different electric fields and multiple antennas, on the near-field positioning performance is evaluated.

**Index Terms**—Cramér-Rao bound, electromagnetic theory, electric field, multiple distributed receiving antennas, near-field positioning, observation capability, performance evaluation.

## I. INTRODUCTION

Real-time and high-accuracy positioning is a crucial component for a large variety of applications, such as autonomous driving, logistics tracking, search-and-rescue, emergency response, Internet-of-Things (IoT), UAV sensing, and emerging integrated sensing and communication (ISAC) [1]–[5]. The 5<sup>th</sup> generation (5G) and beyond networks require the ability of precise positioning, since ubiquitous real-time position information can be extracted by using node-to-node communication capabilities of the network that consists of anchor nodes and agent nodes [6]–[8].

Traditional positioning technologies in the wireless network have been studied extensively. Most of the works exploit either time of arrival (ToA) or direction of arrival (DoA) [9]–[11] measured at the receiver equipped with a single antenna or an antenna array. For time-based estimation, such as ToA or joint DoA and ToA, extremely precise synchronization between the terminal and the receiver must be ensured [12]. As for positioning algorithms, ESPRIT and MUSIC approaches have

been widely proposed to estimate terminal position by using antenna array to observe the channel’s array manifold vector, which is only characterized by DoA. Note that the aforementioned positioning techniques all consider a terminal located in the Fraunhofer (far-field) region<sup>1</sup>, where the wavefront of an electromagnetic (EM) wave transmitted by the terminal can be approximated as a plane wave.

Envisioned as the key features of the beyond 5G networks, adoption of larger antenna arrays or surfaces [14]–[17] and exploitation of higher frequency bands [18]–[20] will push the electromagnetic diffraction field from the far-field region towards the near-field region<sup>2</sup>, in which the wavefront tends to be spherical and the uniform plane wave assumption will no longer hold [22], [23]. Wireless communication taking place in the near-field region provides both new opportunities and challenges for positioning. In particular, the near-field channel’s array manifold vectors contain more information related to the terminal position, as both distance information and DoA information can be inferred from the receiving array. Since traditional positioning technologies are not suitable for near-field positioning, it is critical to develop new architectures and approaches to achieve high-accuracy and high-resolution near-field positioning.

The study of near-field positioning has attracted extensive attention. They can be classified into positioning model design, signal processing algorithm, and performance evaluation. For the model design, reference [24] proposed a model with an imperfectly calibrated array for near-field positioning and studied a calibration method. To simplify the near-field model, many works applied the Fresnel approximation to the antenna arrays with special geometries, e.g., uniform linear arrays (ULAs) [25]–[27], and considered the model mismatch while analyzing the achievable positioning precision. This mismatch inevitably reduced the estimation accuracy [28]. To solve this problem and to characterize the incident waves emitted from a near-field terminal as accurately as possible, the *spherical wavefront model* was developed. An antenna array was utilized to extract the distance and DoA information based on the *spherical wavefront model* and it was revealed that the spherical wavefront provided an underlying generic parametric model for near-field positioning [29]. In [30], the *spherical wavefront model* was extended to a practical scenario with

<sup>1</sup>In the far-field region, the transceiver distance is larger than the Fraunhofer distance  $d_F = 2D^2/\lambda$  [13], where  $D$  is the maximum dimension of the receiving antenna (array), and  $\lambda$  is the wavelength.

<sup>2</sup>In this paper, the term “near-field” refers to the “radiative near-field” and “Fresnel region”, where the transceiver distance is smaller than the Fraunhofer distance, but larger than the Fresnel distance  $d_f = 0.62\sqrt{D^3/\lambda}$  [21].

Ang Chen, Li Chen, and Guo Wei are with the CAS Key Laboratory of Wireless Optical Communication, University of Science and Technology of China, Hefei 230027, China (e-mail: chenang1122@mail.ustc.edu.cn; {chenli87, wei}@ustc.edu.cn).

Yunfei Chen is with the School of Engineering, University of Warwick, Coventry CV4 7AL, U.K. (e-mail: Yunfei.Chen@warwick.ac.uk).

large-scale antenna arrays. The results indicated that terminals in the near-field region could be roughly identified through employing large-scale antenna arrays to estimate the wavefront curvature, i.e., curvature of arrival (CoA). In order to reduce the complexity and implementation cost of large-scale antenna arrays, the authors in [31] introduced the electromagnetic (EM) lens to the *spherical wavefront model*.

Based on the aforementioned *spherical wavefront model*, some works investigated signal processing algorithms for near-field positioning. Reference [32] estimated DoA by using a modified two-dimensional (2-D) MUSIC algorithm and a global-optimum maximum likelihood (ML) searching approach. In [33], a high-order ESPRIT-like algorithm formulated for observations collected from a ULA was proposed. An overlapping symmetric sub-arrays algorithm was proposed in [34] to estimate terminal position with low complexity that did not require computation of high-order statistics in contrast to the traditional near-field ESPRIT algorithm. In [35], a two-stage MUSIC algorithm was proposed to estimate the position of a mixed near-field and far-field terminal. The result indicated that the curvature information should be exploited when the moving terminal approaches the receiver. A subspace-based algorithm without eigendecomposition was proposed in [36], which could provide remarkable and satisfactory estimation performance compared with some existing near-field positioning algorithms. To further reduce the algorithm complexity, the authors in [37] proposed a CoA algorithm. For positioning model utilizing large-scale antenna arrays equipped with EM-lens, an effective parameterized estimation algorithm was proposed in [38], which could directly reuse receiving signals to extract position parameters.

In addition to signal processing, many works have studied the performance evaluation of near-field positioning. In practical scenarios, as the transceived EM waves encounter non-ideal phenomena such as noise, shadowing, and fading, the estimation accuracy of positioning is subject to uncertainty. In the interest of system design and operation, it is momentous to obtain achievable accuracy in positioning operations to provide benchmarks for evaluating performance of the actual positioning systems. The most commonly used tool is the Cramér-Rao bound (CRB), which describes the fundamental lower limits for estimation accuracy. For instance, in [38]–[41], the *spherical wavefront model* was employed to derive the CRBs for the near-field estimator with ULA, planar arrays, or large-scale antenna arrays.

All of the aforementioned works [29]–[41] adopted the *spherical wavefront model*, which has been proved to be inaccurate in [42]. Specifically, the *spherical wavefront model* does not correspond to the equations governing the EM field near an antenna or array, and often disregards the physical characteristics of the near-field source. This could have a profound impact on the generated electromagnetic fields and the observations collected by the receiving antenna. The *analytic model (true model)* is by far the most accurate electromagnetic theory-based model for describing signals in the near-field region. The authors in [43] first evaluated the performance of the near-field positioning system using electromagnetic theory. They computed the CRBs for a terminal located on

the central perpendicular line (CPL) of the receiving antenna surface by using the *vector electric field*. However, in addition to *vector electric field* observation, *scalar electric field* and *overall scalar electric field* observations are also possible due to the different observation capabilities of various receiving antenna paradigms. Moreover, it is more common for the terminal not to be located on the CPL. A more comprehensive study of positioning arbitrary terminal positions by utilizing different electric field observations is necessary. Consequently, it remains unclear how to evaluate the performance of near-field positioning in such a study using the electromagnetic propagation theory and estimation theory.

In this paper, we develop a generic model for near-field positioning. It is also referred to as the general scenario. In this scenario, the receiving antennas<sup>3</sup> with different observation capabilities are employed. This results in the extraction of various electric field observations that require distinct CRB computation methods. In addition, unlike [43], the position of the terminal in front of the receiving antenna is unrestricted such that it can be placed anywhere. A special case when the terminal is on the CPL of the receiving antenna surface is considered. The generality and validity of the generic model are illustrated to obtain further simplifications and insights. Additionally, to show the scaling behavior of the CRBs, two further simplified scenarios are investigated: 1) The system is operating at frequencies in the range of GHz or above; 2) the surface diagonal length of the receiving antenna is significantly greater than the distance from the terminal to the receiver. Finally, the impact of multiple distributed receiving antennas is extensively discussed. The main contributions of this paper are summarized as follows.

- **Utilize analytic model.** Unlike traditional near-field positioning methods following the inaccurate *spherical wavefront model*, an *analytic model* without any approximation is used based on the electromagnetic propagation theory. The CRBs for estimating the terminal position are derived by combining the *analytic model* with the estimation theory to provide fundamental limits for estimation accuracy of the actual near-field positioning system.
- **Generic CRB expressions.** A generic near-field positioning model considering the diversity of observations and the universality of the terminal position is designed. Specifically, three electric fields (*vector*, *scalar* and *overall scalar*) are extracted by receiving antennas with different observation capabilities to derive the generic expressions of CRBs for the terminal with an arbitrary position. This generalizes the existing results in [43]. In the CPL case, the precise closed-form expressions or upper and lower bounds of the CRBs using the *vector* or *scalar electric field* are provided to make it possible to compute and analyze the CRBs in the asymptotic regime.
- **SIMO positioning system.** To investigate the impact of the multiple receiving antennas on the positioning performance, the generic positioning model is extended

<sup>3</sup>In the remainder of our paper, the receiving antenna is a broad concept referring to various antenna paradigms with different observation capabilities, such as a conventional surface antenna and intelligent surfaces with a large number of finely customizable antennas.

to the system with multiple distributed receiving antennas under the CPL assumption, i.e., the single-input multiple-output (SIMO) system and the expressions of CRBs are derived. The results reveal that multiple receiving antennas can significantly improve the estimation accuracy of dimensions parallel to the receiving antenna surface.

The remaining of this paper is organized as follows. Section II describes the generic system model, provides the CRB computation methods using the three electric field observations, and derives the specific CRB expressions. In Section III, the CPL case and two further simplified scenarios are discussed. In Section IV, SIMO positioning system is proposed. Numerical results and discussions are presented in Section V, and the conclusions are given in Section VI.

The following notation is used throughout the paper. Vectors and matrices are denoted in bold lowercase and uppercase respectively, e.g.,  $\mathbf{a}$  and  $\mathbf{A}$ . We use  $[\mathbf{A}]_{ij}$  to denote the  $(i, j)$ th entry of  $\mathbf{A}$  and  $\mathbf{a}_i$  to denote the  $i$ th entry of  $\mathbf{a}$ . The superscripts  $(\cdot)^H$ ,  $(\cdot)^{-1}$ , and  $(\cdot)^T$  represent the matrix hermitian-transpose, inverse, and transpose, respectively.  $(\cdot)^*$  and  $\text{Re}\{\cdot\}$  denote the complex conjugate and real part of the input operations. The operator  $\|\cdot\|$  means to obtain  $\mathcal{L}_2$ -norm of the input and  $|\cdot|$  stands for the modulo operator. The notations  $\mathbb{C}$  and  $\mathbb{R}$  represent sets of complex numbers and of real numbers, respectively.  $n \sim \mathcal{CN}(0, \sigma^2)$  stands for a circularly-symmetric complex-Gaussian random variable with variance  $\sigma^2$ . The notation  $j$  denotes the imaginary unit.  $\mathbf{I}_N$  is the  $N \times N$  identity matrix,  $\mathbf{0}_N$  is the  $N$ -dimensional zero vector, and the suffix  $\kappa = x, y, z$  represents the  $X$ -,  $Y$ - and  $Z$ -dimension in the Cartesian coordinate system, respectively.

## II. SYSTEM MODEL AND CRB COMPUTATION

This section first introduces a generic near-field positioning system aiming to estimate the position of a point source terminal based on the electric field observed over the receiving antenna surface area. Since different receiving antenna settings have different observation capabilities, which are embodied in obtaining different observations, i.e., *vector*, *scalar* and *overall scalar electric field*, we will consider these observations for the near-field positioning system. Finally, we will derive and analyze the CRBs for estimating the terminal position by using the above three electric fields and combining electromagnetic propagation theory with estimation theory.

### A. Generic System Model of Near-field Positioning

Consider the near-field positioning system depicted in Fig. 1. The terminal is a point source equipped with a monochromatic single-antenna located at  $\mathbf{p}_t$  inside a three-dimensional source region  $\mathcal{R}_t$ , and it generates the vector electric field  $\mathbf{e}(\mathbf{p}_r) \in \mathbb{C}^3$  at an arbitrary point  $\mathbf{p}_r$  on the surface  $\mathcal{R}_r$  of the receiving antenna through a homogeneous and isotropic medium with neither scatterers nor reflectors. In order to quantitatively describe the positional relationship between the terminal and receiving antenna, we create two Cartesian coordinate systems,  $OXYZ$  and  $PX'Y'Z'$ , with  $O$  (the center of  $\mathcal{R}_r$ ) and  $\mathbf{p}_t$  (the centroid of  $\mathcal{R}_t$ ) as the origins of the coordinates that have a pure translational relationship. In the

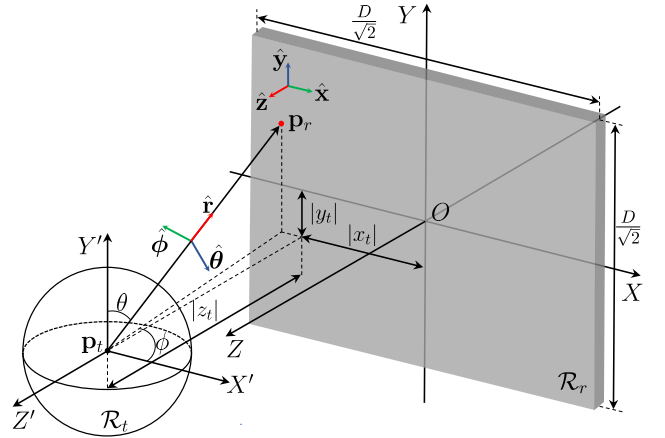


Fig. 1. The generic near-field positioning system.

$OXYZ$  system, we denote  $\mathbf{p}_t = (x_t, y_t, z_t)$ ,  $\mathbf{p}_r = (x_r, y_r, 0)$  and  $\mathcal{R}_r = \{(x_r, y_r, 0) : |x_r| \leq D/\sqrt{8}, |y_r| \leq D/\sqrt{8}\}$ , where  $D$  is the maximum geometric dimension of the receiving antenna, i.e., the diagonal length of the square surface. Since the wavefront is spherical, we establish a spherical coordinate system  $(r, \theta, \phi)$  at point  $\mathbf{p}_t$  to facilitate the description of the spherical wave model.  $\hat{\mathbf{x}}$ ,  $\hat{\mathbf{y}}$ , and  $\hat{\mathbf{z}}$  are unit vectors along the  $X$ -,  $Y$ -, and  $Z$ -dimension in the  $OXYZ$  system while  $\hat{\boldsymbol{\theta}}$  and  $\hat{\boldsymbol{\phi}}$  are unit vectors along the  $\theta$  and  $\phi$  coordinate curves.  $\hat{\mathbf{r}}$  is a unit vector denoting the direction of  $\mathbf{r} = \mathbf{p}_r - \mathbf{p}_t$ .

The near-field positioning system can estimate the position of the terminal by using the electric field observations obtained over the receiving antenna area. Note that depending on the actual communication requirements, cost or technical limitations, the types of receiving antennas may be different, leading to extraction of varying types of observed electric fields and thus affecting the positioning performance. Next, we will introduce three different cases of the electric field observations.

**1) Vector Electric Field (VEF):** The most ideal case is that the *vector electric field* at each point on the whole contiguous surface of the receiving antenna can be observed. To obtain the *VEF*, we apply Holographic MIMO (H-MIMO) [44]–[46] or large intelligent surfaces (LIS) [47]–[49] as the receiving antenna, which is a spatially-contiguous electronically active surface with a vast amount of tiny antenna-elements. In the  $OXYZ$  system, the *vector electric field*  $\mathbf{e}(\mathbf{p}_r)$  can be written as

$$\mathbf{e}(\mathbf{p}_r) = e_x(\mathbf{p}_r)\hat{\mathbf{x}} + e_y(\mathbf{p}_r)\hat{\mathbf{y}} + e_z(\mathbf{p}_r)\hat{\mathbf{z}}. \quad (1)$$

Then, the observation equation using *VEF* is

$$\hat{\mathbf{e}}(\mathbf{p}_r) = \mathbf{e}(\mathbf{p}_r) + \mathbf{n}(\mathbf{p}_r), \quad (2)$$

where  $\hat{\mathbf{e}}(\mathbf{p}_r)$  is the noisy *VEF* and  $\mathbf{n}(\mathbf{p}_r) \in \mathbb{C}^3$  accounts for thermal noise that is distributed as  $\mathbf{n}(\mathbf{p}_r) \sim \mathcal{CN}(\mathbf{0}_3, \sigma^2 \mathbf{I}_3)$ .

**2) Scalar Electric Field (SEF):** If the observation capability of the receiving antenna decreases, there will be a different approach for estimating the position of  $\mathbf{p}_t$ . This method uses a *scalar electric field* that is a component of the Poynting vector perpendicular to each point of the the whole contiguous receiving surface  $\mathcal{R}_r$ . In fact, the *SEF* can be regarded as a scalar approximation to the *VEF* and provide an intermediate



step to understand the *analytic model*. In the *OXYZ* system, the *scalar electric field*  $e(\mathbf{p}_r)$  can be written as

$$e(\mathbf{p}_r) = \sqrt{\|\mathbf{e}(\mathbf{p}_r)\|^2} (-\hat{\mathbf{r}}^T \cdot \hat{\mathbf{z}}) e^{-jk_0 r}, \quad (3)$$

where  $k_0 = \omega/c = 2\pi/\lambda$  is the wave number,  $\omega$  is the angular frequency,  $\lambda$  is the wavelength,  $c$  is the speed-of-light,  $\cdot$  indicates inner product of vectors, and  $r = \|\mathbf{r}\|$ . Then, the observation equation using *SEF* is

$$\hat{e}(\mathbf{p}_r) = e(\mathbf{p}_r) + n(\mathbf{p}_r), \quad (4)$$

where  $\hat{e}(\mathbf{p}_r)$  is the observation of the *SEF* with noise.

**3) Overall Scalar Electric Field (OSEF):** With a further decline in the observation capability of the receiving antenna, we assume that only the *overall scalar electric field* can be obtained, which is the integral of the *scalar electric field*  $e(\mathbf{p}_r)$  over the receiving antenna surface. In this case, the receiving antenna is a conventional surface antenna [50]. According to (3), the *overall scalar electric field*  $e$  is

$$e = \sqrt{\frac{2}{D^2}} \iint_{\mathcal{R}_r} e(\mathbf{p}_r) d\mathbf{p}_r, \quad (5)$$

where  $D^2/2$  is the area of the receiving surface antenna. Then, the observation equation using the *OSEF* is

$$\hat{e} = e + n, \quad (6)$$

where  $\hat{e}$  is the noisy *OSEF*.

Based on the estimation theory, the computation methods of the CRBs for estimating the position of  $\mathbf{p}_t$  using the above three observation equations are given in the following proposition and corollaries.

**Proposition 1** (CRB computation method using *VEF*). Denote the real vector to be estimated as  $\boldsymbol{\xi} \in \mathbb{R}^3 = (x_t, y_t, z_t)$ , which collects the unknown coordinates of  $\mathbf{p}_t$  with respect to the Cartesian system *OXYZ*. The Fisher's Information Matrix (FIM), denoted as  $\mathbf{I}(\boldsymbol{\xi})$ , is a  $3 \times 3$  matrix, whose elements are given by the following double integral:

$$\begin{aligned} [\mathbf{I}(\boldsymbol{\xi})]_{mn} = \frac{2}{\sigma^2} \iint_{\mathcal{R}_r} \text{Re} \left\{ \frac{\partial e_x(\mathbf{p}_r)}{\partial \xi_n} \frac{\partial e_x^*(\mathbf{p}_r)}{\partial \xi_m} + \right. \\ \left. \frac{\partial e_y(\mathbf{p}_r)}{\partial \xi_n} \frac{\partial e_y^*(\mathbf{p}_r)}{\partial \xi_m} + \frac{\partial e_z(\mathbf{p}_r)}{\partial \xi_n} \frac{\partial e_z^*(\mathbf{p}_r)}{\partial \xi_m} \right\} dx_r dy_r, \end{aligned} \quad (7)$$

where  $m, n = 1, 2, 3$ . The CRB for estimating the  $i$ th entry of  $\boldsymbol{\xi}$  is

$$\text{CRB}(\xi_i) = [\mathbf{I}(\boldsymbol{\xi})^{-1}]_{ii}. \quad (8)$$

*Proof:* The results can be derived from [51, Appendix 15C] by replacing the noisy observation and the parameter to be estimated with the complex vector  $\hat{e}(\mathbf{p}_r)$  and the real vector  $\boldsymbol{\xi}$ , respectively. ■

From Proposition 1, the CRBs using *SEF* and *OSEF* can be computed by Corollary 1 and Corollary 2.

**Corollary 1** (CRB computation method using *SEF*). Using the *scalar electric field*, the elements of FIM can be computed as:

$$[\mathbf{I}(\boldsymbol{\xi})]_{mn} = \frac{2}{\sigma^2} \iint_{\mathcal{R}_r} \text{Re} \left\{ \frac{\partial e(\mathbf{p}_r)}{\partial \xi_n} \frac{\partial e^*(\mathbf{p}_r)}{\partial \xi_m} \right\} dx_r dy_r. \quad (9)$$

By substituting (9) into (8), CRBs in this case can be derived.

*Proof:* According to Proposition 1, FIM is additive since  $e_x(\mathbf{p}_r)$ ,  $e_y(\mathbf{p}_r)$ , and  $e_z(\mathbf{p}_r)$  are independent observations. So if we only have one noisy observation  $\hat{e}(\mathbf{p}_r)$ , expression (9) can be derived. ■

**Corollary 2** (CRB computation method using *OSEF*). Similar to Corollary 1, the elements of FIM can be derived as:

$$[\mathbf{I}(\boldsymbol{\xi})]_{mn} = \frac{2}{\sigma^2} \text{Re} \left\{ \frac{\partial e}{\partial \xi_n} \frac{\partial e^*}{\partial \xi_m} \right\}. \quad (10)$$

By substituting (10) into (8), CRBs in this case are obtained.

*Proof:* The only difference between (9) and (10) is that  $e(\mathbf{p}_r)$  has already been integrated in (5). ■

## B. Electric Field Expressions

From the Maxwell equations, the vector electric field  $\mathbf{e}(\mathbf{p}_r)$  generated in the point  $\mathbf{p}_r$  from the isotropic point antenna  $\mathbf{p}_t$  is due to the current density  $\mathbf{J}(\mathbf{p}_t)$  and satisfies [52], [53]

$$\mathbf{E}(\mathbf{p}_r) = \mathbf{G}(\mathbf{r}) \mathbf{J}(\mathbf{p}_t), \quad (11)$$

where  $\mathbf{J}(\mathbf{p}_t)$  is Fourier representation  $\mathbf{J}(\mathbf{p}_t, \omega)$  of the current  $\mathbf{j}(\mathbf{p}_t)$  at point  $\mathbf{p}_t$ .  $\mathbf{G}(\mathbf{r}) \in \mathbb{C}^{3 \times 3}$  is referred as the tensor Green function in electromagnetic theory and can be expressed as

$$\mathbf{G}(\mathbf{r}) \simeq -\frac{j\eta e^{-jk_0 r}}{2\lambda r} (\mathbf{I} - \hat{\mathbf{r}} \cdot \hat{\mathbf{r}}^T), \quad (12)$$

where  $\eta = \sqrt{\mu/\epsilon}$ ,  $\mu$ , and  $\epsilon$  are the permeability, permittivity, and impedance of free-space, respectively. The approximation in (12) is tight when  $r \geq \lambda$ , which always holds when the terminal is in the near-field region (between the reactive near-field and the far-field region) of the receiving antenna [50]. Without loss of generality, we assume that the electromagnetic wave emitted from the terminal  $\mathbf{p}_t$  is polarized in the  $Y$ -dimension, which means that  $\mathbf{J}(\mathbf{p}_t) = J_y(\mathbf{p}_t) \mathbf{e}_y$ .

Using (11) and (12), the specific expressions of the three electric fields *VEF*, *SEF*, and *OSEF* in the near-field region can be obtained by Proposition 2, Corollary 3 and 4.

**Proposition 2** (*Vector electric field*). In the coordinate system *OXYZ*, the three components of the *vector electric field* can be expressed as

$$e_x(\mathbf{p}_r) = jE_0 \frac{(x_r - x_t)(y_r - y_t)}{r^3} e^{-jk_0 r} \quad (13)$$

$$e_y(\mathbf{p}_r) = -jE_0 \frac{1}{r} \left[ 1 - \frac{(y_r - y_t)^2}{r^2} \right] e^{-jk_0 r} \quad (14)$$

$$e_z(\mathbf{p}_r) = -jE_0 \frac{z_t(y_r - y_t)}{r^3} e^{-jk_0 r}, \quad (15)$$

where  $E_0 = \frac{\eta J_y(\mathbf{p}_t)}{2\lambda}$  is initial electric intensity and is measured in volts (V).

*Proof:* Please see Appendix A. ■

**Corollary 3** (*Scalar electric field*). In the coordinate system *OXYZ*, the *scalar electric field* can be derived as

$$e(\mathbf{p}_r) = E_0 \frac{\sqrt{z_t[(x_r - x_t)^2 + z_t^2]}}{r^{5/2}} e^{-jk_0 r}. \quad (16)$$

*Proof:* Substituting (64) in Appendix A into (3) yields

$$e(\mathbf{p}_r) = \sqrt{\|\mathbf{G}(\mathbf{r})\mathbf{J}(\mathbf{p}_t)\|^2 \sin\theta \sin\phi} e^{-jk_0 r}. \quad (17)$$

By using (71) – (73) in Appendix A into (17), the *scalar electric field* with respect to  $(r, \theta, \phi)$  can be expressed as

$$e(\mathbf{p}_r) = |G(r)|J_y(\mathbf{p}_t) \sqrt{\sin^3\theta \sin\phi} e^{-jk_0 r}. \quad (18)$$

By substituting (74) – (76) in Appendix A into (18) yields Corollary 3. ■

**Corollary 4** (*Overall scalar electric field*). In the coordinate system  $OXYZ$ , the *overall scalar electric field* is

$$e = E_0 \sqrt{\frac{2}{D^2}} \iint_{\mathcal{R}_r} \frac{\sqrt{z_t[(x_r - x_t)^2 + z_t^2]}}{r^{5/2}} e^{-jk_0 r} dx_r dy_r. \quad (19)$$

*Proof:* From (5) and (18), the overall scalar observation is derived in Corollary 4. ■

### C. CRB Computation and Analysis

Using results in Sec. II-A and II-B, the expressions of the CRBs for estimating the position of  $\mathbf{p}_t$  in Fig. 1 are provided.

**Proposition 3** (CRB expressions,  $\mathbf{e}(\mathbf{p}_r)$ ). Using the *vector electric field*, the CRBs can be computed as

$$\text{CRB}_1(x_t) = \frac{\text{SNR}^{-1}}{2} \cdot \frac{-I_{23}^2 + I_{22}I_{33}}{I_s} \quad (20)$$

$$\text{CRB}_1(y_t) = \frac{\text{SNR}^{-1}}{2} \cdot \frac{-I_{13}^2 + I_{11}I_{33}}{I_s} \quad (21)$$

$$\text{CRB}_1(z_t) = \frac{\text{SNR}^{-1}}{2} \cdot \frac{-I_{12}^2 + I_{11}I_{22}}{I_s}, \quad (22)$$

where  $\text{SNR} = |E_0|^2/\sigma^2$ ,  $I_{mn} = \rho_{11}^{mn} + \rho_{12}^{mn}$ ,  $m \leq n$ ,  $\rho_{11}^{mn}$  and  $\rho_{12}^{mn}$  are computed in (81) – (92) in Appendix B, and

$$I_s = 2I_{12}I_{13}I_{23} + I_{11}I_{22}I_{33} - I_{13}^2I_{22} - I_{11}I_{23}^2 - I_{12}^2I_{33}.$$

*Proof:* According to Proposition 1 and Proposition 2, the first-order derivatives  $\partial h_x(\mathbf{p}_r)/\partial x_t, \dots, \partial h_z(\mathbf{p}_r)/\partial z_t$  in FIM, where  $h_\kappa(\mathbf{p}_r) \triangleq e_\kappa(\mathbf{p}_r)/E_0$ , are first computed. For their specific expressions, please see (80a) – (80i) in Appendix B. Then by substituting these expressions into (7), we can derive the elements of FIM as follows.

$$[\mathbf{I}(\boldsymbol{\xi})]_{mn} = 2\text{SNR}(\rho_{11}^{mn} + \rho_{12}^{mn}). \quad (23)$$

Since FIM is a symmetric matrix, we have  $[\mathbf{I}(\boldsymbol{\xi})]_{mn, m \neq n} = [\mathbf{I}(\boldsymbol{\xi})]_{nm, m \neq n}$ . By applying the matrix inversion lemma, we obtain the inverse of  $\mathbf{I}(\boldsymbol{\xi})$ , denoted as  $\mathbf{I}(\boldsymbol{\xi})^{-1}$ , whose diagonal elements are the CRBs for estimating  $x_t$ ,  $y_t$ , and  $z_t$ . ■

Based on the above expressions of the CRBs for *VEF*, the CRBs for *SEF* and *OSEF* are provided in the following Corollary 5 and Corollary 6.

**Corollary 5** (CRB expressions,  $\mathbf{e}(\mathbf{p}_r)$ ). If using the *scalar electric field* observation, the specific expressions of the CRBs can also be computed by (20) – (22), and we denote them as  $\text{CRB}_2(\kappa_t)$ . The only difference from Proposition 3 is the

computation of  $I_{mn}$ , where  $I_{mn} = \rho_{21}^{mn} + \rho_{22}^{mn} \cdot \rho_{21}^{mn}$  and  $\rho_{22}^{mn}$  are given in (94) – (105) in Appendix B.

*Proof:* According to Corollary 3, the first-order derivatives  $\partial h(\mathbf{p}_t)/\partial \kappa_t$  involved in FIM  $\mathbf{I}(\boldsymbol{\xi})$ , where  $h(\mathbf{p}_t) \triangleq e(\mathbf{p}_t)/E_0$ , are computed in (93a) – (93c) in Appendix B. According to Corollary 1,  $\text{CRB}_2(\kappa_t)$  can be derived. ■

**Corollary 6** (CRB expressions,  $e$ ). If we can only obtain the *overall scalar electric field* observation. The CRBs, denoted as  $\text{CRB}_3(\kappa_t)$ , can also be computed by (20) – (22), but the expression of  $I_{mn}$  is different. Specifically,  $I_{mn} = \rho_3^{mn}$ ,

$$\rho_3^{mn} = \frac{2}{D^2} \text{Re} \left\{ \frac{\partial h}{\partial \xi_n} \frac{\partial h^*}{\partial \xi_m} \right\}, \quad (24)$$

and  $h \triangleq \frac{D}{\sqrt{2}} e/E_0$ .

*Proof:* The results can be derived based on Corollary 2 and Corollary 4. ■

Note that it might be difficult to compute the value of  $\rho_3^{mn}$  due to the double integral in the molecule of partial derivative  $\partial h/\partial \kappa_t$  in (24). By approximating the integral as a summation, a simpler expression of  $\rho_3^{mn}$  can be obtained. In particular, we divide the receiving surface  $\mathcal{R}_r$  into  $\alpha$  parts, where  $\sqrt{\alpha}$  is a positive integer and an odd number for simplicity. Denote the coordinate of each small part as  $(x_i, y_j)$ , where  $x_i$  is the arithmetic sequence  $(x_1, x_2, \dots, x_{\sqrt{\alpha}})$ , the common difference is  $\frac{D}{\sqrt{2\alpha}}$ , and the first item is  $x_1 = \frac{D}{2\sqrt{2\alpha}} - \frac{D}{2\sqrt{2}}$ . Similarly, the arithmetic sequence  $y_j$  has the same common difference and the first item as  $x_i$ . So  $h$  can be written approximately as  $h_d$ ,

$$h_d = \frac{D^2}{2\alpha} \sum_{i=1}^{\sqrt{\alpha}} \sum_{j=1}^{\sqrt{\alpha}} \frac{\sqrt{z_t[(x_i - x_t)^2 + z_t^2]}}{r_{i,j}^{5/2}} e^{-jk_0 r_{i,j}}, \quad (25)$$

where  $r_{i,j} = \sqrt{(x_i - x_t)^2 + (y_j - y_t)^2 + z_t^2}$ . Therefore,  $\rho_3^{mn}$  can be computed by  $\frac{2}{D^2} \text{Re} \left\{ \frac{\partial h_d}{\partial \xi_n} \frac{\partial h_d^*}{\partial \xi_m} \right\}$ . Further, the specific expressions of  $\rho_3^{mn}$  are given in (106) – (111) in Appendix B.

## III. CRB FOR A TRANSMITTER ON THE CPL

To validate the results derived in Sec. II-C, a simplified case of the generic near-field positioning system is considered, where the terminal is on the CPL of the receiving antenna surface. Specifically, the CPL is the line perpendicular to the receiving antenna surface  $\mathcal{R}_r$  passing through the centre point  $O$  and the three-dimensional source region  $\mathcal{R}_t$  degenerates into the one-dimensional region  $\mathcal{L}_t$ , as shown in Fig. 2.

### A. CRB Computation and Analysis for CPL Case

In CPL case, we have  $x_t = y_t = 0$  (but they are unknown), and  $r = \sqrt{x_r^2 + y_r^2 + z_t^2}$ . Since  $r$  is an even function with respect to  $x_r$  and  $y_r$ , and the integration domain  $\mathcal{R}_r$  is symmetric, the cross-terms of different dimensions in the FIM  $\mathbf{I}(\boldsymbol{\xi})$  are zero, meaning that the FIM  $\mathbf{I}(\boldsymbol{\xi})$  is a diagonal matrix. Using the properties of the diagonal matrix inversion, the process of computing CRBs will be greatly simplified.

We denote a parameter  $\tau \triangleq D/z_t$ , which measures the diagonal length of the receiving antenna surface normalized

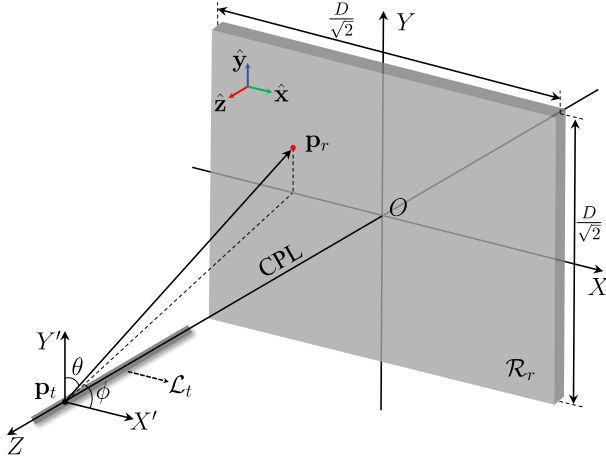


Fig. 2. The near-field positioning system for CPL case.

by the distance from the considered terminal position to the receiver. For a terminal in the near-field region, the value of  $\tau$  is large, and for a terminal far away from the receiving antenna,  $\tau$  becomes small. Then we define a new integration domain  $\mathcal{R}_\tau = \{(u, v) : |u| \leq \tau/\sqrt{8}, |v| \leq \tau/\sqrt{8}\}$ .

Based on Proposition 3, Corollary 5, and Corollary 6, the following results can be obtained.

**Corollary 7 (CRB, VEF, CPL).** If the terminal is on the CPL, the CRBs for the estimation of  $x_t$ ,  $y_t$ , and  $z_t$  using the *vector electric field*, denoted as  $\text{CRB}_1^C(\kappa_t)$ , are

$$\text{CRB}_1^C(\kappa_t) = \frac{\text{SNR}^{-1}}{2(k_0^2 \rho_{11\kappa} + z_t^{-2} \rho_{12\kappa})}, \quad (26)$$

where

$$\rho_{11x} \triangleq \iint_{\mathcal{R}_\tau} \frac{u^2(u^2+1)}{(u^2+v^2+1)^3} dudv \quad (27)$$

$$\rho_{12x} \triangleq \iint_{\mathcal{R}_\tau} \frac{u^4+v^4+u^2+v^2-u^2v^2}{(u^2+v^2+1)^4} dudv \quad (28)$$

$$\rho_{11y} \triangleq \iint_{\mathcal{R}_\tau} \frac{v^2(u^2+1)}{(u^2+v^2+1)^3} dudv \quad (29)$$

$$\rho_{12y} \triangleq \iint_{\mathcal{R}_\tau} \frac{(u^2+1)(u^2+4v^2+1)}{(u^2+v^2+1)^4} dudv \quad (30)$$

$$\rho_{11z} \triangleq \iint_{\mathcal{R}_\tau} \frac{u^2+1}{(u^2+v^2+1)^3} dudv \quad (31)$$

$$\rho_{12z} \triangleq \iint_{\mathcal{R}_\tau} \frac{v^4+u^2v^2+1}{(u^2+v^2+1)^4} dudv. \quad (32)$$

*Proof:* Since FIM  $\mathbf{I}(\xi)$  is a diagonal matrix, (8) can be rewritten as

$$\text{CRB}(\xi_i) = [\mathbf{I}(\xi)]_{ii}^{-1} = I_{ii}^{-1}, \quad (33)$$

where  $I_{ii} = \rho_{11}^{ii} + \rho_{12}^{ii}$ ,  $\rho_{11}^{ii}$  and  $\rho_{12}^{ii}$  can be computed by replacing  $x_{r,t}$  and  $y_{r,t}$  in (81) – (86) with  $x_t$  and  $y_t$ . ■

**Remark 1** (The generalizability of proposition 3). Proposition 3 can be simplified to Corollary 7 by utilizing diagonal matrix inversion and simplification of  $\rho_{11}^{11} - \rho_{12}^{33}$  when the terminal is on the CPL. Besides, the expressions of  $\text{CRB}_1^C(\kappa_t)$  are

consistent with the results in [43, Eqs. (28)–(36)]. The only difference is that we have replaced the integration variables  $x_t$  and  $y_t$  with  $u$  and  $v$  for a more intuitive analysis of the effect of  $\lambda$  and  $z_t$  on the CRBs. Consequently, the expressions of the CRBs (using the *vector electric field*) in proposition 3 are more general than [43]. In fact, compared with the CPL case, Sec. II-A provides a generic positioning model.

**Remark 2** (Closed-form expressions of  $\text{CRB}_1^C(\kappa_t)$ ). Different from [43, Eqs. (39)–(46)], the more precise closed-form expressions for  $\rho_{12x}$ ,  $\rho_{12y}$ ,  $\rho_{11z}$ , and  $\rho_{12z}$  are given in (112) – (115) in Appendix C. Since the closed-form expressions of  $\rho_{11x}$  and  $\rho_{11y}$  are hard to obtain, their closed-form upper and lower bounds are provided in (118) – (121).

**Corollary 8 (CRB, SEF, CPL).** For the CPL case, the CRBs for estimating  $x_t$ ,  $y_t$ , and  $z_t$  using the *scalar electric field*, denoted as  $\text{CRB}_2^C(\kappa_t)$ , are given by

$$\text{CRB}_2^C(\kappa_t) = \frac{\text{SNR}^{-1}}{2(k_0^2 \rho_{21\kappa} + z_t^{-2} \rho_{22\kappa})}, \quad (34)$$

where

$$\rho_{21x} \triangleq \iint_{\mathcal{R}_\tau} \frac{u^2(u^2+1)}{(u^2+v^2+1)^{7/2}} dudv \quad (35)$$

$$\rho_{22x} \triangleq \iint_{\mathcal{R}_\tau} \frac{u^2(3u^2-2v^2+3)^2}{4(u^2+1)(u^2+v^2+1)^{9/2}} dudv \quad (36)$$

$$\rho_{21y} \triangleq \iint_{\mathcal{R}_\tau} \frac{v^2(u^2+1)}{(u^2+v^2+1)^{7/2}} dudv \quad (37)$$

$$\rho_{22y} \triangleq \iint_{\mathcal{R}_\tau} \frac{25v^2(u^2+1)}{4(u^2+v^2+1)^{9/2}} dudv \quad (38)$$

$$\rho_{21z} \triangleq \iint_{\mathcal{R}_\tau} \frac{u^2+1}{(u^2+v^2+1)^{7/2}} dudv \quad (39)$$

$$\rho_{22z} \triangleq \iint_{\mathcal{R}_\tau} \frac{(u^4+u^2v^2+3v^2-u^2-2)^2}{4(u^2+1)(u^2+v^2+1)^{9/2}} dudv. \quad (40)$$

*Proof:* The diagonal elements of FIM  $\mathbf{I}(\xi)$  in (33) can be written as  $I_{ii} = \rho_{21}^{ii} + \rho_{22}^{ii}$ ,  $\rho_{21}^{ii}$  and  $\rho_{22}^{ii}$  can be computed by replacing  $x_{r,t}$  and  $y_{r,t}$  in (94) – (99) with  $x_t$  and  $y_t$ . ■

The closed-form expressions of  $\rho_{21\kappa}$  and  $\rho_{22\kappa}$  are complicated and lengthy, so we provided their closed-form upper and lower bounds in (123) – (134).

Corollary 7 and Corollary 8 clearly demonstrate the effects of the wavelength  $\lambda = 2\pi/k_0$  and the propagation distance  $d = z_t$  on the CRBs for fixed values of  $\tau$  and SNR in the near-field positioning system (using the *vector* or *scalar electric field*). In particular, the CRBs for all dimensions decrease as  $\lambda$  or  $z_t$  decreases. In other words, the estimation accuracy of the positioning system increases as the carrier frequency ( $f_c$ ) becomes higher or as the propagation distance becomes closer.

**Corollary 9 (CRB, OSEF, CPL).** When we use the *overall scalar electric field*, the CRBs for the CPL case, denoted as  $\text{CRB}_3^C(\kappa_t)$ , can be computed as follows.

$$\text{CRB}_3^C(\kappa_t) = \frac{\text{SNR}^{-1}}{\frac{4}{D^2} |\rho_{3\kappa}|^2}, \quad (41)$$

where  $\rho_{3\kappa} \triangleq \frac{\partial h}{\partial \kappa_t}$ . Utilize  $h_d$  to discretize  $h$ , we have

$$\text{CRB}_3^C(\kappa_t) \approx \frac{\frac{\alpha^2}{D^2} \text{SNR}^{-1}}{\left| \sum_{i=1}^{\sqrt{\alpha}} \sum_{j=1}^{\sqrt{\alpha}} f_{iz} \rho_{3\kappa}^{i,j} e^{-jk_0 r_{i,j}} \right|^2}, \quad (42)$$

where  $f_{iz} \triangleq \sqrt{z_t(x_i^2 + z_t^2)}$  and

$$\rho_{3x}^{i,j} \triangleq x_i \left( jk_0 r_{i,j}^{-\frac{7}{2}} + \frac{5}{2} r_{i,j}^{-\frac{9}{2}} - \frac{1}{z_t^2 + x_i^2} r_{i,j}^{-\frac{5}{2}} \right) \quad (43)$$

$$\rho_{3y}^{i,j} \triangleq y_j \left( jk_0 r_{i,j}^{-\frac{7}{2}} + \frac{5}{2} r_{i,j}^{-\frac{9}{2}} \right) \quad (44)$$

$$\rho_{3z}^{i,j} \triangleq -jk_0 z_t r_{i,j}^{-\frac{7}{2}} - \frac{5}{2} z_t r_{i,j}^{-\frac{9}{2}} + \frac{3z_t^2 + x_i^2}{2f_{iz}^2} r_{i,j}^{-\frac{5}{2}}. \quad (45)$$

*Proof:* The results can be derived utilizing Corollary 6 and equation (25) following the property of the inverse of a diagonal matrix  $\mathbf{I}(\xi)$ . ■

**Remark 3** ( $\text{CRB}_2^C(\kappa_t) < \text{CRB}_3^C(\kappa_t)$ ). We can either compute (42) numerically or use the Cauchy-Schwarz inequality to show

$$\begin{aligned} \text{CRB}_3^C(\kappa_t) &> \frac{\frac{\alpha^2}{D^2} \text{SNR}^{-1}}{\sum_{i=1}^{\sqrt{\alpha}} \sum_{j=1}^{\sqrt{\alpha}} \alpha \left| f_{iz} \rho_{3\kappa}^{i,j} e^{-jk_0 r_{i,j}} \right|^2} \\ &= \frac{\text{SNR}^{-1}}{\frac{D^2}{\alpha} \sum_{i=1}^{\sqrt{\alpha}} \sum_{j=1}^{\sqrt{\alpha}} \left( k_0^2 \rho_{21\kappa}^{i,j} + z_t^{-2} \rho_{22\kappa}^{i,j} \right)} \\ &= \text{CRB}_2^C(\kappa_t), \end{aligned} \quad (46)$$

where  $\rho_{21\kappa}^{i,j}$  and  $\rho_{22\kappa}^{i,j}$  are the discretized sampling of the integrand in (35) – (40). It can be seen that, under the same condition, the CRBs using *SEF* are the lower bounds of the CRBs using *OSEF*. Using *OSEF* can significantly reduce the complexity of the near-field positioning system, but at the cost of reduced estimation accuracy.

## B. Two Further Simplified Scenarios

1) *CRB analysis for  $z_t \gg \lambda$* : Consider a scenario where the distance from the terminal located on the CPL to the receiver is much larger than the wavelength, namely  $z_t \gg \lambda^4$ . It generally holds in wireless communication systems with frequencies in the range of GHz ( $10^9$  Hz) or above. Expressions of the CRBs in Corollary 7 and 8 can be further simplified as follows.

**Corollary 10** (CRB, CPL,  $z_t \gg \lambda$ ). If  $z_t \gg \lambda$ , the CRBs for the CPL case can be further simplified as

a) Using the *vector electric field*,  $\text{CRB}_1^C(\kappa_t)$  reduces to

$$\text{CRB}_1^C(\kappa_t) \approx \frac{\text{SNR}^{-1}}{2k_0^2 \rho_{11\kappa}}. \quad (47)$$

b) Using the *scalar electric field*,  $\text{CRB}_2^C(\kappa_t)$  reduces to

$$\text{CRB}_2^C(\kappa_t) \approx \frac{\text{SNR}^{-1}}{2k_0^2 \rho_{21\kappa}}. \quad (48)$$

*Proof:* Please refer to Appendix D. ■

<sup>4</sup> $z_t \gg \lambda$  corresponds to the near-field region when the size of the receiving antenna is on the order of meters, because  $z_t \ll 2D^2/\lambda$  when  $z_t \gg \lambda$  and  $D$  is not very small.

Corollary 10 shows that, when  $z_t \gg \lambda$ , the CRBs for all dimensions are solely determined by the values of  $\lambda$  and  $\tau$ . Particularly, if we keep  $\tau$  and SNR fixed,  $\text{CRB}_1^C(\kappa_t)$  and  $\text{CRB}_2^C(\kappa_t)$  are proportional to the square of  $\lambda$ . Furthermore, for a fixed value of  $\tau$ , if  $z_t$  increases by a factor  $\alpha$ , the surface diagonal length  $D$  needs to be scaled by the same factor  $\alpha$  (the surface area of the receiving antenna increases by the factor  $\alpha^2$ ) to keep the CRBs unchanged.

**Remark 4** (Comparison of estimation accuracy). From Corollary 7 and Corollary 8, we find that  $\rho_{11\kappa} > \rho_{12\kappa}$ . Accordingly, based on Corollary 10 and Remark 3, we derive that

$$\text{CRB}_1^C(\kappa_t) < \text{CRB}_2^C(\kappa_t) < \text{CRB}_3^C(\kappa_t). \quad (49)$$

Inequality (49) shows that using the *vector electric field* at each point on the receiving surface renders lower CRBs, i.e., higher estimation accuracy. Using the *scalar electric field* will reduce the complexity of the observations, but the CRBs will increase. If the conventional surface antenna is employed as the receiver, the near-field positioning system can only obtain the *overall scalar electric field*, which will further reduce the complexity of the system but the accuracy decreases too.

2) *Asymptotic CRB analysis for  $\tau \rightarrow \infty$* : Based on the above analysis, it is interesting to analyze the behaviour of the asymptotic CRBs when the surface diagonal length  $D$  is much larger than the distance  $z_t$  from the terminal to the receiver. Corollary 11 gives the CRBs in the asymptotic regime  $\tau \rightarrow \infty$ .

**Corollary 11** (CRB, CPL,  $\tau \rightarrow \infty$ ). For the CPL case and  $z_t \gg \lambda$ , in the asymptotic regime  $\tau \rightarrow \infty$ , the CRBs for the estimation of  $x_t$ ,  $y_t$ , and  $z_t$  are given by

a) Using the *vector electric field*, we have

$$\lim_{\tau \rightarrow \infty} \text{CRB}_1^C(x_t) = \frac{\text{SNR}^{-1} \lambda^2}{6\pi^3 \ln \tau} \quad (50)$$

$$\lim_{\tau \rightarrow \infty} \text{CRB}_1^C(y_t) = \frac{\text{SNR}^{-1} \lambda^2}{2\pi^3 \ln \tau} \quad (51)$$

$$\lim_{\tau \rightarrow \infty} \text{CRB}_1^C(z_t) = \frac{\text{SNR}^{-1}}{6\pi^3} \lambda^2. \quad (52)$$

b) Using the *scalar electric field*, we have

$$\lim_{\tau \rightarrow \infty} \text{CRB}_2^C(x_t) = \frac{15}{64} \frac{\text{SNR}^{-1}}{\pi^3} \lambda^2 \quad (53)$$

$$\lim_{\tau \rightarrow \infty} \text{CRB}_2^C(y_t) = \frac{15}{32} \frac{\text{SNR}^{-1}}{\pi^3} \lambda^2 \quad (54)$$

$$\lim_{\tau \rightarrow \infty} \text{CRB}_2^C(z_t) = \lim_{\tau \rightarrow \infty} \text{CRB}_2^C(x_t). \quad (55)$$

*Proof:* We have provided the closed-form expressions or upper and lower bounds in Appendix C, making it possible to compute and analyze the asymptotic CRBs. By computing the limit values of (118) and (119), we have that  $\rho_{11x} \sim \frac{3\pi}{4} \ln \tau$  for  $\tau \rightarrow \infty$ . According to (120) and (121), we have that  $\rho_{11y} \sim \frac{\pi}{4} \ln \tau$  for  $\tau \rightarrow \infty$ . Similarly, according to (114) and (123) – (132), we have  $\lim_{\tau \rightarrow \infty} \rho_{11z} = \frac{3\pi}{4}$ ,  $\lim_{\tau \rightarrow \infty} \rho_{21x} = \frac{8\pi}{15}$ ,  $\lim_{\tau \rightarrow \infty} \rho_{21y} = \frac{4\pi}{15}$  and  $\lim_{\tau \rightarrow \infty} \rho_{21z} = \frac{8\pi}{15}$ , where we use  $\lim$  to represent  $\lim_{\tau \rightarrow \infty}$ . Thus, Corollary 11 holds. ■

From Corollary 11, the following observations can be made. Firstly, for the near-field positioning system, if we use the *vector electric field*, the CRBs for estimating  $x_t$  and  $y_t$  will



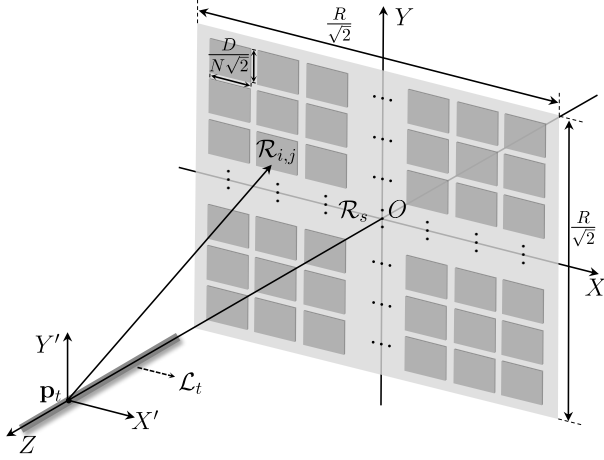


Fig. 3. The SIMO near-field positioning system.

decrease as a  $\ln^{-1}$  function of  $\tau$  and go to zero as  $\tau$  increases infinitely. But  $\text{CRB}_1^C(z_t)$  tends to a fixed value which depends uniquely on the  $\lambda$  and SNR, and does not change with  $\tau$ . In the CPL case,  $z_t$  represents the propagation distance, so equation (52) provides a fundamental lower limit to the near-field ranging precision. Secondly, if we use the *scalar electric field*, the CRBs for the estimation of  $x_t$  and  $z_t$  are identical and the three CRBs are solely determined by  $\lambda$  and SNR as  $\tau$  increases. Finally, in order to get more insights on the difference of fundamental limit of the estimation accuracy between *VEF* and *SEF* as  $\tau$  increases, we denote their difference as  $\Delta C_\kappa = p_\kappa \text{SNR}^{-1} \lambda^2$  with  $p_x = 15/(64\pi^3) \approx 7.56 \times 10^{-3}$ ,  $p_y = 15/(32\pi^3) \approx 1.512 \times 10^{-2}$ , and  $p_z = 13/(192\pi^3) \approx 6.77 \times 10^{-5}$ . This indicates that using *SEF* has a smaller performance penalty for the estimation of  $z_t$  than  $x_t$  and  $y_t$  compared to using *VEF*.

#### IV. CRB OF THE SIMO POSITIONING SYSTEM

The receiving antenna in the previous sections is a single antenna or intelligent surface<sup>5</sup>, where the positioning system can be defined as the single-input single-output (SISO) system. In this section, the system with multiple distributed receiving antennas will be discussed, referred to as the single-input multiple-output (SIMO) system depicted in Fig. 3. This SIMO system is specifically interpreted as follows.

- **Space constraints:** Each of the small receiving antenna is an intelligent surface or conventional surface antenna as previously described and they are distributed on a large rectangular surface  $\mathcal{R}_s$  with size  $\frac{R}{\sqrt{2}} \times \frac{R}{\sqrt{2}}$ , where  $R$  is usually a fixed value (a few meters to tens of meters) due to space constraints<sup>6</sup> of the positioning system.
- **Total surface area:** The total surface area is the same for different numbers of the small receiving antennas and each of them has the same surface area and properties. In

<sup>5</sup>The single intelligent surface represents a *centralized-deployment* LIS/H-MIMO, which can observe *VEF/SEF*. Besides, the single antenna corresponds to a conventional surface antenna and it can only obtain *OSEF*. For simplicity, we define both of them as “single-output”.

<sup>6</sup>The receiving antenna, such as LIS, can be easily embedded in daily life objects with limited size such as buildings, walls, cars, etc.

particular, we consider that the total surface area is  $\frac{D^2}{2}$  and the number of the receiving antennas is  $N^2$ . Therefore, the size of each receiving antenna is  $\frac{D}{N\sqrt{2}} \times \frac{D}{N\sqrt{2}}$ .

- **Terminal position:** For simplicity, the terminal is located on the CPL with coordinates  $(0, 0, z_t)$ , which makes the FIM matrix diagonalize as will be shown in Lemma 1.

Note that if  $N = 1$ , the SIMO system degenerates into the SISO system, where the CRBs for all three dimensions using the three electric fields have been computed and analyzed in Sec. II-B and Sec. III. In this section, we assume  $N \geq 2$ . To derive the CRBs of the SIMO system, we provide Lemma 1.

**Lemma 1** (Properties of the Fisher’s information). The FIM of the SIMO system is a diagonal matrix, and the Fisher’s information is identical for every four small receiving antennas rotationally symmetric about the origin (rotation angle is  $90^\circ$ ).

*Proof:* Since  $\rho_{11}^{12} - \rho_{12}^{23}$  in (87) – (92) and  $\rho_{21}^{12} - \rho_{22}^{23}$  in (100) – (105) (items in FIM off-diagonal elements) contain at least an odd power term of either  $x_r$  or  $y_r$ , and  $r$  is an even function with respect to  $x_r$  and  $y_r$ , we can prove that even though the integral domains of  $\rho_{11}^{12} - \rho_{12}^{23}$  and  $\rho_{21}^{12} - \rho_{22}^{23}$  are no longer symmetric about the origin, due to the additivity of the Fisher’s information, there can be a symmetric integral of each integral whose sum is zero. Consequently, the off-diagonal elements of the FIM matrix are canceled. Similarly,  $\rho_{11}^{11} - \rho_{33}^{33}$  in (81) – (86) and  $\rho_{21}^{11} - \rho_{32}^{33}$  in (94) – (99) (items in FIM diagonal elements) contain even power terms of  $x_r$  and/or  $y_r$ , so the diagonal elements are non-zero, and the values of  $\rho_{11}^{11} - \rho_{33}^{33}$  and  $\rho_{21}^{11} - \rho_{32}^{33}$  remain unchanged if  $x_r$  becomes  $-x_r$  and/or  $y_r$  becomes  $-y_r$ . Therefore, Lemma 1 holds. ■

Based on Lemma 1, we divide the large rectangular surface into four equal parts using the  $X$  and  $Y$  axes as their boundaries. Then, we only need to study one of the four parts, which contains  $\frac{N^2}{4}$  small receiving antennas with index  $(i, j)$ ,  $i, j = 1, \dots, \frac{N}{2}$ . The integral domain of the small receiving antenna with index  $(i, j)$  is denoted as  $\mathcal{R}_{i,j} = (x_r, y_r, 0)$ , where  $x_r \in [\frac{(2i-1)R-D}{2\sqrt{2}N}, \frac{(2i-1)R+D}{2\sqrt{2}N}]$ ,  $y_r \in [\frac{(2j-1)R-D}{2\sqrt{2}N}, \frac{(2j-1)R+D}{2\sqrt{2}N}]$ . Additionally,  $\mathcal{R}_{i,j}$  can be rewritten as  $\mathcal{R}_{i,j}^\tau = (u, v, 0)$ , where  $u \in \frac{1}{2\sqrt{2}N}[\frac{(2i-1)R}{z_t} - \tau, \frac{(2i-1)R}{z_t} + \tau]$ ,  $v \in \frac{1}{2\sqrt{2}N}[\frac{(2j-1)R}{z_t} - \tau, \frac{(2j-1)R}{z_t} + \tau]$ . The CRBs of the SIMO positioning system using *VEF*, *SEF* and *OSEF* are derived as follows.

**Proposition 4** (CRB, SIMO). For the defined SIMO positioning system depicted in Fig. 3, we have that:

- Using the *vector electric field*, the CRBs can be given by

$$\text{CRB}_1^M(\kappa_t) = \frac{\text{SNR}^{-1}}{8 \sum_{j=1}^{\frac{N}{2}} \sum_{i=1}^{\frac{N}{2}} \left( k_0^2 \rho_{11\kappa}^{i,j} + z_t^{-2} \rho_{12\kappa}^{i,j} \right)}, \quad (56)$$

where  $\rho_{11\kappa}^{i,j}$ ,  $\rho_{12\kappa}^{i,j}$  have the same integrand as  $\rho_{11\kappa}$ ,  $\rho_{12\kappa}$  in (27) – (32), but their integral domain is  $\mathcal{R}_{i,j}^\tau$ .

- Using the *scalar electric field*, the CRBs are given by

$$\text{CRB}_2^M(\kappa_t) = \frac{\text{SNR}^{-1}}{8 \sum_{j=1}^{\frac{N}{2}} \sum_{i=1}^{\frac{N}{2}} \left( k_0^2 \rho_{21\kappa}^{i,j} + z_t^{-2} \rho_{22\kappa}^{i,j} \right)}, \quad (57)$$

where  $\rho_{21\kappa}^{i,j}$ ,  $\rho_{22\kappa}^{i,j}$  have the same integrand as  $\rho_{21\kappa}$ ,  $\rho_{22\kappa}$  in (35) – (40), but their integral domain is  $\mathcal{R}_{i,j}^\tau$ .



c) Using the *overall scalar electric field*, the CRBs are

$$\text{CRB}_3^M(\kappa_t) = \frac{\text{SNR}^{-1}}{\frac{16}{D^2} \sum_{j=1}^{\frac{N}{2}} \sum_{i=1}^{\frac{N}{2}} \left| \rho_{3\kappa}^{ij} \right|^2}, \quad (58)$$

where  $\rho_{3\kappa}^{ij} = \frac{\partial h_{ij}}{\partial \kappa_t}$ ,  $h_{ij}$  has the same integrand as  $h$  in Corollary 6 while its integral domain is  $\mathcal{R}_{i,j}$ . According to (42), the more feasible expression of (58) is given. Similarly, we divide each small receiving surface  $\mathcal{R}_{i,j}$  into  $\alpha$  parts, and denote that  $x_{m,i} = \frac{(2i-1)R-D}{2\sqrt{2N}} + \frac{(2m-1)D}{2\sqrt{2\alpha N}}$ ,  $y_{n,j} = \frac{(2j-1)R-D}{2\sqrt{2N}} + \frac{(2n-1)D}{2\sqrt{2\alpha N}}$ ,  $r_{mn,ij} = \sqrt{x_{m,i}^2 + y_{n,j}^2 + z_t^2}$ , then  $\text{CRB}_3^M(\kappa_t)$  can be further written as follows.

$$\text{CRB}_3^M(\kappa_t) \approx \frac{\frac{\alpha^2}{4D^2} \text{SNR}^{-1}}{\sum_{j=1}^{\frac{N}{2}} \sum_{i=1}^{\frac{N}{2}} \left| \sum_{m=1}^{\sqrt{\alpha}} \sum_{n=1}^{\sqrt{\alpha}} \varrho_{3\kappa}^{mn,ij} \right|^2}, \quad (59)$$

where  $\varrho_{3\kappa}^{mn,ij} = \sqrt{z_t(x_{m,i}^2 + z_t^2)} \rho_{3\kappa}^{mn,ij} e^{-jk_0 r_{mn,ij}}$  and  $\rho_{3\kappa}^{mn,ij}$  is given in (43) – (45), but  $x_i, y_j$  and  $r_{i,j}$  need to be modified to  $x_{m,i}, y_{n,j}$  and  $r_{mn,ij}$ , respectively.

*Proof:* Corollary 7 – 9 have computed the CRBs for all three dimensions using the three electric fields in the SISO positioning system and the crux of the computation is to give the values of double integrals  $\rho_{11\kappa}, \rho_{12\kappa}, \rho_{21\kappa}, \rho_{22\kappa}$  and  $\rho_{3\kappa}$ , whose domain is  $\mathcal{R}_\tau$  or  $\mathcal{R}_r$ . In the SIMO positioning system, since the domain of each small receiving antenna is different and discontinuous, we change the domains from  $\mathcal{R}_\tau/\mathcal{R}_r$  to  $\mathcal{R}_{i,j}^\tau/\mathcal{R}_{i,j}$ . Moreover, the electric field observations of each small receiving antennas are independent. So the Fisher's information is additive. Hence, Proposition 4 holds. ■

Proposition 4 indicates that  $\text{CRB}_1^M(\kappa_t)$  and  $\text{CRB}_2^M(\kappa_t)$  decrease as  $\lambda$  or  $z_t$  decreases for fixed values of  $N$  and  $\tau$  or, equivalently, of the functions  $\rho_{ab\kappa}^{i,j}, a, b = 1, 2$ . The impact of the number  $N^2$  of small receiving antennas on the CRBs will be investigated in Sec. V-C. Note that, same as Remark 3,  $\text{CRB}_2^M(\kappa_t)$  can be verified as the lower bounds of the  $\text{CRB}_3^M(\kappa_t)$  by using the Cauchy-Schwarz inequality.

The authors in [48] use the scalar field observed from LIS to derive the CRBs in the SIMO positioning system. They consider a simple and idealized radiation model, which overlooks the physical characteristics of the source. Besides, they assume that the terminal is in the far-field to simplify the computation of CRBs. In Proposition 4, we derive CRBs of the SIMO near-field positioning system while considering the characteristics of the near-field source and using different electric fields.

Next, we analyze the behaviour of the CRBs in the SIMO positioning system when  $z_t \gg \tau$  and  $\tau \rightarrow \infty$ . The main results are summarized in the following two corollaries.

**Corollary 12** (SIMO,  $z_t \gg \tau$ ). If  $z_t \gg \lambda$ , the CRBs of the SIMO positioning system can be simplified as

$$\text{CRB}_1^M(\kappa_t) \approx \frac{\text{SNR}^{-1}}{8 \sum_{j=1}^{\frac{N}{2}} \sum_{i=1}^{\frac{N}{2}} k_0^2 \rho_{11\kappa}^{i,j}} \quad (60)$$

$$\text{CRB}_2^M(\kappa_t) \approx \frac{\text{SNR}^{-1}}{8 \sum_{j=1}^{\frac{N}{2}} \sum_{i=1}^{\frac{N}{2}} k_0^2 \rho_{21\kappa}^{i,j}}. \quad (61)$$

*Proof:* We can show that: 1)  $\rho_{11\kappa}^{i,j} > \rho_{12\kappa}^{i,j}$  or  $\rho_{11\kappa}^{i,j}$  has the same order of magnitude as  $\rho_{12\kappa}^{i,j}$ ; 2) both of them are positive. Then,  $k_0^2 \rho_{11\kappa}^{i,j} \gg z_t^2 \rho_{12\kappa}^{i,j}$  for  $z_t \gg \lambda$ . Similarly, we can show that  $k_0^2 \rho_{21\kappa}^{i,j} \gg z_t^2 \rho_{22\kappa}^{i,j}$  for  $z_t \gg \lambda$ . Thus, expression (56) and (57) can be simplified to (60) and (61). ■

Note that  $\text{CRB}_1^M(\kappa_t) < \text{CRB}_2^M(\kappa_t) < \text{CRB}_3^M(\kappa_t)$  can be derived based on Corollary 12, which is similar to inequality (49). It clearly indicates that using multiple distributed receiving antennas does not affect the order of estimation accuracy of using different electric field observations.

**Corollary 13** (SIMO,  $\tau \rightarrow \infty$ ). If  $z_t \gg \lambda$  and  $\tau \rightarrow \infty$ , the CRBs of the SIMO positioning system can be given by

$$\lim_{\tau \rightarrow \infty} \text{CRB}_1^M(\kappa_t) = \lim_{\tau \rightarrow \infty} \text{CRB}_1^C(\kappa_t)/N^2 \quad (62)$$

$$\lim_{\tau \rightarrow \infty} \text{CRB}_2^M(\kappa_t) = \lim_{\tau \rightarrow \infty} \text{CRB}_2^C(\kappa_t)/N^2. \quad (63)$$

*Proof:* The results can be derived based on Corollary 11 and Corollary 12. Particularly, we have that  $\lim_{\tau \rightarrow \infty} \rho_{11\kappa}^{i,j} = \lim_{\tau \rightarrow \infty} \rho_{11\kappa}$  and  $\lim_{\tau \rightarrow \infty} \rho_{21\kappa}^{i,j} = \lim_{\tau \rightarrow \infty} \rho_{21\kappa}$ , where we use  $\lim$  to represent  $\lim_{\tau \rightarrow \infty}$ . Thus, Corollary 13 holds. ■

It can be seen from Corollary 13 that the CRBs of the SIMO positioning system will be one- $N^2$ th of the SISO system as  $\tau$  increases unboundedly. On the large surface with fixed size, different small receiving antennas will be stacked on top of each other with  $\tau$  increasing, resulting in multiplexing benefits and lower CRBs. Besides, the total area of the small receiving antennas will be larger than  $\mathcal{R}_s$  as  $\tau \rightarrow \infty$ , which ignores the space constraints. In fact, the more practical and meaningful case is  $\tau \leq R/z_t$ , which will be analyzed in Sec. V-C.

## V. NUMERICAL RESULTS AND DISCUSSIONS

In this section, we will provide numerical results to illustrate the propositions and corollaries that we have derived in previous sections. We set the signal-to-noise ratio as  $\text{SNR} = |E_0|^2/\sigma^2 = -10\text{dB}$  and the wavelength as  $\lambda = 0.01m$  (corresponding to  $f_c = 30\text{GHz}$ ) unless otherwise specified.

### A. CRB Evaluation for CPL Case

We first show the CRBs for a terminal on the CPL computed in Sec. III. In order to illustrate the influence of the system carrier frequency on the CRBs, we consider two different values of the wavelength, i.e.,  $\lambda = 0.01m$  and  $\lambda = 0.001m$  (corresponding to  $f_c = 300\text{GHz}$ ). Fig. 4 and Fig. 5 demonstrate the CRBs, measured in square meters [ $m^2$ ], versus the surface diagonal length  $D$  or the distance from the terminal to the receiving antenna (terminal-surface distance)  $d = z_t$  when  $z_t = 6m$  or  $D = 9m$ , respectively.

It can be seen from Fig. 4 that all the CRBs decrease dramatically with the surface diagonal length in the range  $1m \leq D \leq 10m$ , which contains the values of  $D$  commonly used in the practical system. In addition, the CRBs for  $z_t$  are much lower than those for  $x_t$  and  $y_t$  in the above range. More interestingly, the CRBs using *SEF* are greater than CRBs using *VEF* for all values of  $D$ , which agrees with Remark 4. The difference between  $\text{CRB}_1(\kappa_t)$  and  $\text{CRB}_2(\kappa_t)$  is negligible when  $D \leq 10m$ , but it will increase gradually with the increase of  $D$ . As for the CRBs in the asymptotic regime, we find that:

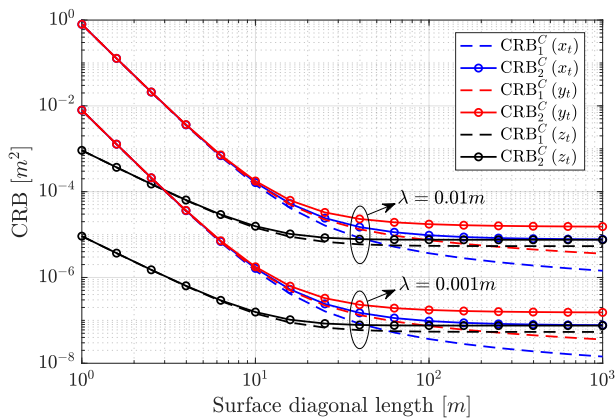


Fig. 4. CRBs versus surface diagonal length  $D$ , with  $\lambda = 0.01m$  or  $0.001m$ ,  $z_t = 6m$ , when  $\mathbf{p}_t$  is on the CPL and using *VEF* or *SEF*.

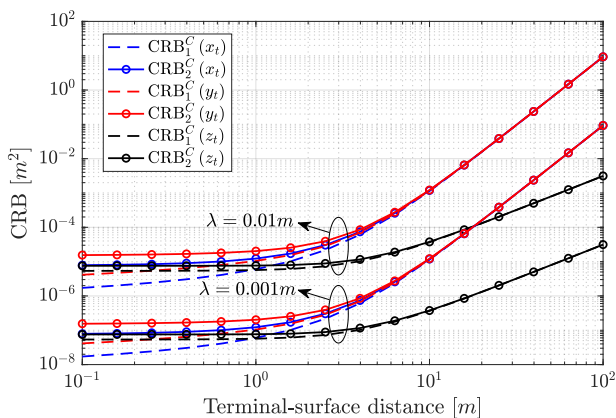


Fig. 5. CRBs versus terminal-surface distance  $z_t$ , with  $D = 9m$ ,  $\lambda = 0.01m$  or  $0.001m$ , when  $\mathbf{p}_t$  is on the CPL and using *VEF* or *SEF*.

1)  $\text{CRB}_1(x_t)$  and  $\text{CRB}_1(y_t)$  decrease unboundedly with the trend of the  $\ln^{-1}$  function in (50) and (51); 2)  $\text{CRB}_1(z_t)$  and  $\text{CRB}_2(z_t)$  approach the asymptotic limit in (52) and (55) from  $D \approx 20m$ ; 3)  $\text{CRB}_2(x_t)$  and  $\text{CRB}_2(y_t)$  converge to the asymptotic limit in (53) and (54) when  $D > 10^3m$ . These phenomena are consistent with Corollary 11. Fig. 5 shows that the CRBs for all the dimensions increase very slowly with the terminal-surface distance in the range  $0.1m \leq z_t \leq 1m$ , but they increase considerably (among them,  $\text{CRB}_1^C(z_t)$  and  $\text{CRB}_2^C(z_t)$  are much lower than the CRBs for  $x_t$  and  $y_t$ ) when  $z_t > 1m$ . It is worth noting that all the CRBs depend linearly on  $\lambda^2$  regardless of *VEF* or *SEF*, as in Corollary 10.

Table I provides the square root of the CRBs (RCRB, denoted as  $R(\kappa_t)$ ), measured in centimeters [cm], for the three components  $x_t$ ,  $y_t$ , and  $z_t$ , for terminals located on the CPL.  $D_1$ ,  $D_2$ ,  $D_3$ , and  $D_4$  represent that the surface diagonal length is  $0.5m$ ,  $1m$ ,  $2m$ , and  $3m$  when  $z_t = 6m$ , respectively. To evaluate the average positioning performance, we use the receiving antenna with  $D = 3m$  to compute the average RCRB of 1000 terminals with coordinates of  $z_t$  dimension uniformly distributed in  $[1m, 20m]$ , which is denoted as *Ave*. It can be seen that using *VEF* or *SEF* can guarantee a centimeter-level accuracy (within a few centimeters) for estimating all three dimensions in the mmWave or sub-THz bands. This is in

TABLE I  
COMPARISON OF ESTIMATION ACCURACY BETWEEN USING *VEF*, *SEF*, AND *OSEF* (- MEANS THE VALUE IS TOO LARGE).

		RCRB [cm]				
		$D_1$	$D_2$	$D_3$	$D_4$	<i>Ave</i>
<i>VEF</i>	$R(x_t)$	35.5	8.91	2.25	1.02	<b>3.88</b>
	$R(y_t)$	35.5	8.91	2.26	1.02	<b>3.88</b>
	$R(z_t)$	0.604	0.303	0.153	0.103	<b>0.179</b>
<i>SEF</i>	$R(x_t)$	35.5	8.92	2.26	1.03	<b>3.89</b>
	$R(y_t)$	35.6	8.92	2.26	1.03	<b>3.89</b>
	$R(z_t)$	0.605	0.303	0.153	0.104	<b>0.179</b>
<i>OSEF</i>	$R(x_t)$	-	-	-	-	-
	$R(y_t)$	-	-	-	-	-
	$R(z_t)$	11.8	21.1	20.4	23.7	<b>18.0</b>

contrast with the results in [43]. Unfortunately, we find that, even though an accuracy on the order of tens of centimeters in  $Z$ -dimension can be achieved by using *OSEF*, we are unable to estimate  $x_t$  and  $y_t$  with an acceptable accuracy. This reveals that a single conventional surface antenna possesses only the near-field ranging function, which can be considered a one-dimensional special case of near-field positioning.

### B. CRB Evaluation for the General Scenario

Next, we will evaluate the CRBs for a terminal not on the CPL as discussed in Proposition 3, Corollary 5 and 6. Fig. 6 illustrates the CRBs as a function of the distance  $d = \sqrt{x_t^2 + y_t^2 + z_t^2}$  for a terminal at  $(2, 3, z_t)$  when  $D = 9m$ . It can be found that the estimation accuracy reduces as the terminal-surface distance increases, which is consistent with our intuition. Particularly, the CRBs for estimating  $x_t$  and  $y_t$  increase faster than  $z_t$  regardless of *VEF* or *SEF*. Furthermore, all the CRBs increase rapidly when the terminal is close to the receiving antenna ( $0 < z_t \leq \sqrt{3}m$ ). This occurs because the estimation for all dimensions is nearly perfect (CRB is approaching 0) when the terminal approaches the receiving antenna ( $z_t \rightarrow 0$ ,  $|x_t|$  and  $|y_t|$  are less than  $\frac{D}{2\sqrt{2}}$ ), and as  $z_t$  increases from 0, CRBs will rapidly increase to greater orders of magnitude. Besides, we find that  $\text{CRB}_2(\kappa_t)$  is greater than  $\text{CRB}_1(\kappa_t)$  when the terminal-surface distance is less than  $10m$ , otherwise they are equal. This indicates that for a receiving antenna with fixed size, there is a considerable performance gap between *VEF* and *SEF*, only when the terminal is close to the receiving antenna.

Fig. 7 illustrates the CRBs for terminals with different  $x_t$  and  $y_t$  versus the terminal-surface distance when using *SEF*,  $D = 9m$  and  $\lambda = 0.001m$ . It shows that the CRBs have different trends and the curve shapes vary from each other for different  $x_t$  and  $y_t$  when the terminal is close to the receiving antenna. For instance, if the terminal is on the CPL ( $x_t = y_t = 0$ ,  $d = z_t$ ), the CRBs for all dimensions are almost unchanged in the range  $0.1m < d < 1m$ . However, if  $x_t$  or  $y_t$  are greater than  $\frac{D}{2\sqrt{2}}$  and  $z_t$  is small, which means the vertical projection of the terminal along the  $Z$ -dimension is not on the receiving antenna surface and the distance from the terminal to the CPL is much larger than  $z_t$ , the CRBs sharply decrease from infinity. We refer this phenomenon as the near-

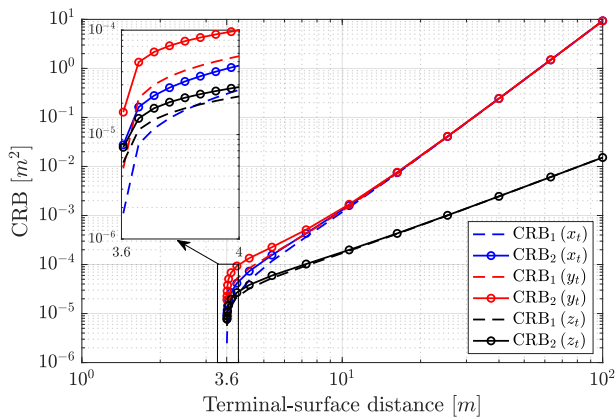


Fig. 6. CRBs as a function of the terminal-surface distance for a terminal at  $(2, 3, z_t)$  when using *VEF* or *SEF*, and  $D = 9m$ .

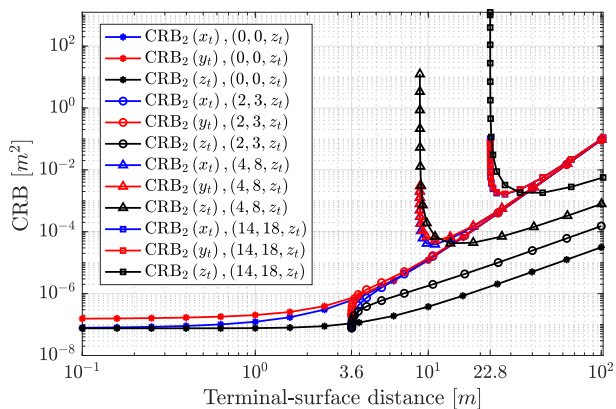


Fig. 7. CRBs as a function of the terminal-surface distance for terminals with different  $x_t$  and  $y_t$  when using *SEF*,  $D = 9m$  and  $\lambda = 0.001m$ . Since using *VEF* or *SEF* has the same rules, we take the use of *SEF* as an example.

field positioning *blocking zone* effect, which always exists for a fixed-size receiving surface antenna. Notably, extensive numerical simulations in Fig. 4 for terminals not on the CPL demonstrate that results obtained in the analysis of the CPL case in Sec. III are also applicable to the generic near-field positioning system proposed in Sec. II, which provides support for the generalizability of our insights and results.

Fig. 8 demonstrates the normalized CRBs for the terminal not on the CPL, versus  $x_t$  and  $y_t$  when  $z_t = 6m$ ,  $D = 3m$ , and using *VEF* or *SEF*. These normalized CRBs, measured in [dB] and denoted as  $\text{CRB}_1^N(\kappa_t)$  and  $\text{CRB}_2^N(\kappa_t)$ , are defined as the values of CRBs normalized by their minimum, which can be achieved when the terminal is on the CPL ( $x_t = y_t = 0$ ). In order to clearly illustrate the different behaviours of the CRBs when the terminal moves away from the CPL, the color of the point  $(x_t, y_t)$  is used to measure the normalized CRB values corresponding to that point. In particular, the normalized CRB values are mapped to the color gamut, where warmer colors represent higher values and lower values are associated to cooler colors. It can be seen that the CRB for estimating  $z_t$  increases faster than those for  $x_t$  and  $y_t$  regardless of using *VEF* or *SEF*. In addition, the maximum normalized values of  $\text{CRB}_1(\kappa_t)$  (as shown in Fig. 8a, 8c and 8e) and  $\text{CRB}_2(\kappa_t)$  (as

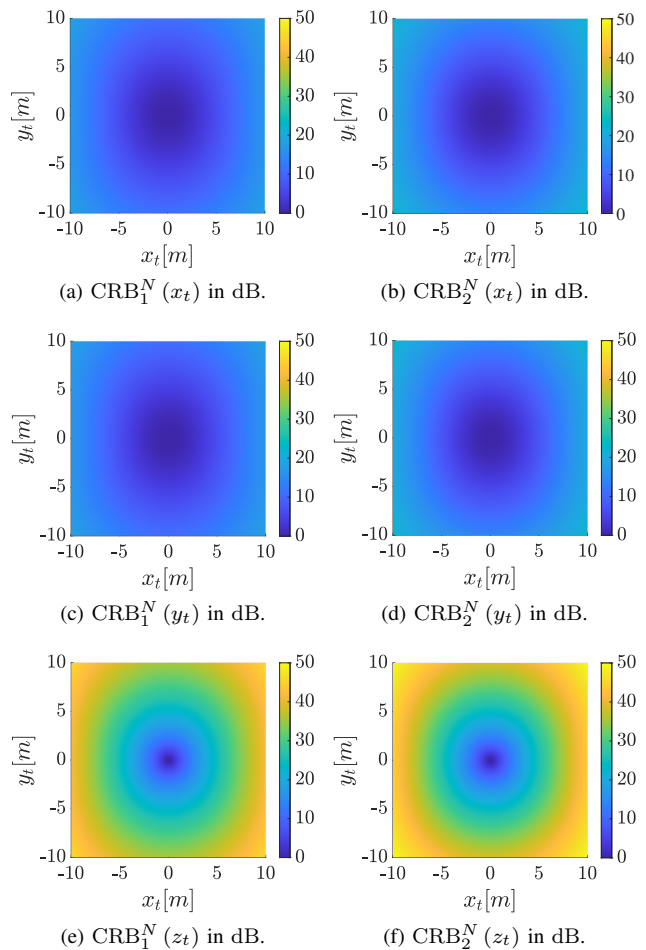


Fig. 8. Normalized CRBs, measured in [dB], as a function of  $x_t$  and  $y_t$  for the terminal not on the CPL when using *VEF/SEF*,  $z_t = 6m$  and  $D = 3m$ . We have that  $\text{CRB}_1^N(\kappa_t) = 10 \log_{10}[\text{CRB}_1(\kappa_t)/\text{CRB}_1^C(\kappa_t)]$  and  $\text{CRB}_2^N(\kappa_t) = 10 \log_{10}[\text{CRB}_2(\kappa_t)/\text{CRB}_2^C(\kappa_t)]$ .

shown in Fig. 8b, 8d and 8f) are 18.40dB, 18.41dB, 45.68dB, 22.41dB, 22.42dB, and 49.69dB, respectively. This result indicates that the CRBs using *SEF* have a more significant increase than those using *VEF*, and the difference is about 4dB for all dimensions.

### C. CRB Evaluation for the SIMO Positioning System

Finally, we will evaluate the CRBs for the SIMO positioning system as discussed in Sec. IV. We set  $R = 30m$ ,  $z_t = 6m$  and  $\lambda = 0.001m$ . Based on Proposition 4, we compare the CRBs for a terminal on the CPL with different number of small receiving antennas, i.e.,  $N^2 = 1, 4, 16, 64, 256$ .

As shown in Fig. 9, when  $D > R$ , the SIMO positioning system renders lower CRBs than the SISO positioning system for all three dimensions. More precisely,  $\text{CRB}_1^M(\kappa_t)$  will be one- $N^2$ th of  $\text{CRB}_1^C(\kappa_t)$  as  $D$  increases infinitely, as in Corollary 13. Due to the space constraints, we are more interested in the range  $D \leq R$ , where the surface area covered by the small receiving antennas will be smaller than the large rectangular surface  $\mathcal{R}_s$ . It can be seen that the CRBs for estimating  $x_t$  and  $y_t$  are significantly improved when using the SIMO system in the above range of practical interest, although the CRBs for  $z_t$  become worse. For instance, the CRBs for  $x_t$  and  $y_t$



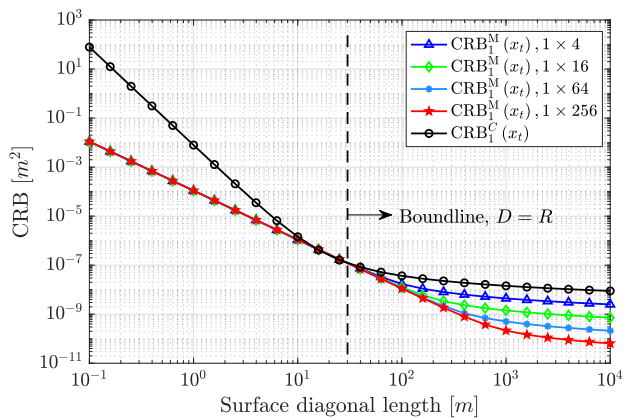
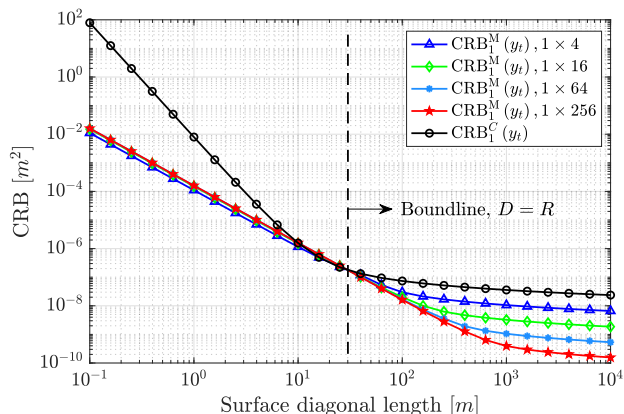
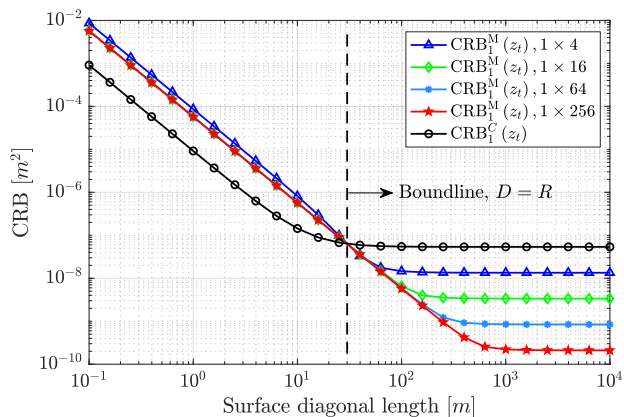
(a)  $\text{CRB}_1^M(x_t)$  and  $\text{CRB}_1^C(x_t)$  versus  $D$ .(b)  $\text{CRB}_1^M(y_t)$  and  $\text{CRB}_1^C(y_t)$  versus  $D$ .(c)  $\text{CRB}_1^M(z_t)$  and  $\text{CRB}_1^C(z_t)$  versus  $D$ .

Fig. 9. CRBs with different number of small receiving antennas ( $N^2 = 1, 4, 16, 64, 256$ , equivalently expressed as  $\text{CRB}_1^C(\kappa_t)$ ,  $1 \times 4, 1 \times 16, 1 \times 64, 1 \times 256$ ) with  $R = 30m$ ,  $z_t = 6m$ , and  $\lambda = 0.001m$  when using *VEF*.

with 4 small receiving antennas, each antenna has a surface diagonal length  $0.025m$ , can achieve the same CRBs for a single receiving antenna with  $D \approx 0.9m$ , that is, the antenna surface area needed for estimating  $X$ - and  $Y$ -dimension by the SIMO positioning system is only 1.23% of that by the SISO system when  $D$  is small. The CRB for estimating  $z_t$  with 4 small receiving antennas is around 10dB larger than  $\text{CRB}_1^C(z_t)$  when  $D$  is the same and less than  $10m$ . Besides, we find that  $\text{CRB}_1^M(x_t)$  remains the same when the number

of small receiving antennas changes, whereas  $\text{CRB}_1^M(y_t)$  is slightly lower when  $N^2 = 4$  compared to  $N^2 = 16, 64, 256$ , and  $\text{CRB}_1^M(z_t)$  is slightly larger when  $N^2 = 4$ . In fact, to achieve cooperation and coupling calibration among the small receiving antennas, more stringent hardware is required as the number of small antennas rises. Therefore, in light of the performance of the positioning system and the cost of hardware, the SIMO positioning system with 4 small receiving antennas is the superior option for estimating  $x_t$  and  $y_t$ , whereas the SISO system is the better choice for estimating  $z_t$ , i.e., ranging. It is worth noting that using *SEF* in the SIMO system has the same rules as using *VEF*. Using *OSEF* in the SIMO system with 4 small antennas still fails to estimate the three coordinates of the terminal, but when the number of small receiving antennas is large enough, using *OSEF* can be approximated as using *SEF*.

## VI. CONCLUSIONS

In this paper, a generic near-field positioning model considering different electric field observations and the universality of the terminal position has been proposed. With the purpose of evaluating the estimation accuracy of this system, we have combined electromagnetic propagation theory with estimation theory to develop generic CRB expressions for three Cartesian coordinates of the terminal. Three electric fields (*vector*, *scalar* and *overall scalar electric field*) have been studied for various antenna paradigms with varying observation capabilities. The derived CRB expressions generalize the existing results in [43], where the terminal is located on the CPL of the receiving antenna surface and the *vector electric field* is utilized. As a result of the CPL assumption, simplifications and insights have been obtained, as well as closed-form CRB expressions. The correlation between estimation precision and observation capability has been discovered. Additionally, the generic CPL model has been expanded to account for systems with multiple distributed receiving antennas, and its optimal estimation precision has been thoroughly discussed. Asymptotic expressions of the CRBs have been provided to illustrate their scaling behaviors in relation to carrier frequency and surface diagonal length. Numerical results have shown that centimeter-level accuracy can be achieved in the near-field of a receiving antenna of a practical size in the mmWave or sub-THz bands by using the *vector* or *scalar electric field*. The *overall scalar electric field* observed by a conventional surface antenna can only be used for ranging. Furthermore, the multiple receiving antennas enhance the estimation accuracy of dimensions parallel to the receiving antenna surface.

## APPENDIX A PROOF OF PROPOSITION 2

The transformation relationship between the basis vectors  $\hat{r}$ ,  $\hat{\theta}$ ,  $\hat{\phi}$  of the spherical coordinate system  $(r, \theta, \phi)$  and the basis vectors  $\hat{x}$ ,  $\hat{y}$ ,  $\hat{z}$  of the Cartesian coordinate system  $OXYZ$  is

$$\hat{r} = \sin \theta \cos \phi \hat{x} + \cos \theta \hat{y} - \sin \theta \sin \phi \hat{z} \quad (64)$$

$$\hat{\theta} = \cos \theta \cos \phi \hat{x} - \sin \theta \hat{y} - \cos \theta \sin \phi \hat{z} \quad (65)$$

$$\hat{\phi} = -\sin \phi \hat{x} - \cos \phi \hat{z}. \quad (66)$$



Plugging (64) into (11) and (12) yields

$$e_x(\mathbf{p}_r) = G(r) \left[ (1 - \sin^2 \theta \cos^2 \phi) J_x(\mathbf{p}_t) - (\sin \theta \cos \phi \cos \theta) J_y(\mathbf{p}_t) + (\sin^2 \theta \cos \phi \sin \phi) J_z(\mathbf{p}_t) \right] \quad (67)$$

$$e_y(\mathbf{p}_r) = G(r) \left[ (-\sin \theta \cos \theta \cos \phi) J_x(\mathbf{p}_t) + \sin^2 \theta J_y(\mathbf{p}_t) + (\sin \theta \cos \theta \sin \phi) J_z(\mathbf{p}_t) \right] \quad (68)$$

$$e_z(\mathbf{p}_r) = G(r) \left[ (\sin^2 \theta \sin \phi \cos \phi) J_x(\mathbf{p}_t) + (\sin \theta \cos \theta \sin \phi) J_y(\mathbf{p}_t) + (1 - \sin^2 \theta \sin^2 \phi) J_z(\mathbf{p}_t) \right], \quad (69)$$

where  $\mathbf{J}(\mathbf{p}_t) = J_x(\mathbf{p}_t) \hat{\mathbf{x}} + J_y(\mathbf{p}_t) \hat{\mathbf{y}} + J_z(\mathbf{p}_t) \hat{\mathbf{z}}$ , and  $G(r)$  is the scalar Green function

$$G(r) = -\frac{j\eta e^{-jk_0 r}}{2\lambda r}. \quad (70)$$

Since we assume that the electromagnetic wave is polarized in the  $Y$ -dimension, (67) – (69) can be simplified as

$$e_x(\mathbf{p}_r) = G(r) (-\sin \theta \cos \phi \cos \theta) J_y(\mathbf{p}_t) \quad (71)$$

$$e_y(\mathbf{p}_r) = G(r) \sin^2 \theta J_y(\mathbf{p}_t) \quad (72)$$

$$e_z(\mathbf{p}_r) = G(r) (\sin \theta \cos \theta \sin \phi) J_y(\mathbf{p}_t). \quad (73)$$

The dependence of  $e_x(\mathbf{p}_r)$ ,  $e_y(\mathbf{p}_r)$  and  $e_z(\mathbf{p}_r)$  on the position  $(x_t, y_t, z_t)$  is hidden in  $(r, \theta, \phi)$ . We have

$$r = \sqrt{(x_r - x_t)^2 + (y_r - y_t)^2 + z_t^2}, \quad (74)$$

$$\cos \theta = \frac{y_r - y_t}{r}, \quad (75)$$

$$\tan \phi = \frac{z_t}{x_r - x_t}. \quad (76)$$

from which it follows that

$$\sin \theta \cos \theta \cos \phi = \frac{(x_r - x_t)(y_r - y_t)}{r^2}, \quad (77)$$

$$\sin^2 \theta = 1 - \frac{(y_r - y_t)^2}{r^2}, \quad (78)$$

$$\sin \theta \cos \theta \sin \phi = \frac{z_t(y_r - y_t)}{r^2}. \quad (79)$$

By substituting (70) and (77) – (79) into (71) – (73) yields Proposition 2.

## APPENDIX B SOME COMPLEX EXPRESSIONS

In the proof of Proposition 3, we should compute some first-order derivatives to derive the elements of FIM  $\mathbf{I}(\boldsymbol{\xi})$ , and the specific expressions are as follows.

$$\frac{\partial h_x(\mathbf{p}_r)}{\partial x_t} = x_{r,t} y_{r,t} \left( \frac{3j}{r^5} - \frac{j}{x_{r,t}^2 r^3} - \frac{k_0}{r^4} \right) e^{-jk_0 r} \quad (80a)$$

$$\frac{\partial h_x(\mathbf{p}_r)}{\partial y_t} = x_{r,t} y_{r,t}^2 \left( \frac{3j}{r^5} - \frac{j}{y_{r,t}^2 r^3} - \frac{k_0}{r^4} \right) e^{-jk_0 r} \quad (80b)$$

$$\frac{\partial h_x(\mathbf{p}_r)}{\partial z_t} = x_{r,t} y_{r,t} z_t \left( -\frac{3j}{r^5} + \frac{k_0}{r^4} \right) e^{-jk_0 r} \quad (80c)$$

$$\frac{\partial h_y(\mathbf{p}_r)}{\partial x_t} = x_{r,t} \left( j \frac{3y_{r,t}^2 - r^2}{r^5} - k_0 \frac{y_{r,t}^2 - r^2}{r^4} \right) e^{-jk_0 r} \quad (80d)$$

$$\frac{\partial h_y(\mathbf{p}_r)}{\partial y_t} = y_{r,t} \left( j \frac{3y_{r,t}^2 - 3r^2}{r^5} - k_0 \frac{y_{r,t}^2 - r^2}{r^4} \right) e^{-jk_0 r} \quad (80e)$$

$$\frac{\partial h_y(\mathbf{p}_r)}{\partial z_t} = z_t \left( j \frac{-3y_{r,t}^2 + r^2}{r^5} + k_0 \frac{y_{r,t}^2 - r^2}{r^4} \right) e^{-jk_0 r} \quad (80f)$$

$$\frac{\partial h_z(\mathbf{p}_r)}{\partial x_t} = x_{r,t} y_{r,t} z_t \left( -\frac{3j}{r^5} + \frac{k_0}{r^4} \right) e^{-jk_0 r} \quad (80g)$$

$$\frac{\partial h_z(\mathbf{p}_r)}{\partial y_t} = y_{r,t}^2 z_t \left( -\frac{3j}{r^5} + \frac{j}{y_{r,t}^2 r^3} + \frac{k_0}{r^4} \right) e^{-jk_0 r} \quad (80h)$$

$$\frac{\partial h_z(\mathbf{p}_r)}{\partial z_t} = y_{r,t} z_t^2 \left( \frac{3j}{r^5} - \frac{j}{z_t^2 r^3} - \frac{k_0}{r^4} \right) e^{-jk_0 r}, \quad (80i)$$

where we have set  $x_{r,t} = x_r - x_t$  and  $y_{r,t} = y_r - y_t$ .

The specific expressions of  $\rho_{11}^{mn}$  and  $\rho_{12}^{mn}$  are as follows.

$$\rho_{11}^{11} = k_0^2 \iint_{\mathcal{R}_r} \frac{x_{r,t}^2 (x_{r,t}^2 + z_t^2)}{r^6} dx_r dy_r \quad (81)$$

$$\rho_{12}^{11} = \iint_{\mathcal{R}_r} \frac{(x_{r,t}^2 + y_{r,t}^2) r^2 - 3x_{r,t}^2 y_{r,t}^2}{r^8} dx_r dy_r \quad (82)$$

$$\rho_{11}^{22} = k_0^2 \iint_{\mathcal{R}_r} \frac{y_{r,t}^2 (x_{r,t}^2 + z_t^2)}{r^6} dx_r dy_r \quad (83)$$

$$\rho_{12}^{22} = \iint_{\mathcal{R}_r} \frac{(x_{r,t}^2 + z_t^2)(x_{r,t}^2 + z_t^2 + 4y_{r,t}^2)}{r^8} dx_r dy_r \quad (84)$$

$$\rho_{11}^{33} = k_0^2 z_t^2 \iint_{\mathcal{R}_r} \frac{x_{r,t}^2 + z_t^2}{r^6} dx_r dy_r \quad (85)$$

$$\rho_{12}^{33} = \iint_{\mathcal{R}_r} \frac{y_{r,t}^2 (r^2 - 2z_t^2) + z_t^2 (z_t^2 + x_{r,t}^2)}{r^8} dx_r dy_r \quad (86)$$

$$\rho_{11}^{12} = k_0^2 \iint_{\mathcal{R}_r} \frac{x_{r,t} y_{r,t} (x_{r,t}^2 + z_t^2)}{r^6} dx_r dy_r \quad (87)$$

$$\rho_{12}^{12} = \iint_{\mathcal{R}_r} \frac{x_{r,t} y_{r,t} (x_{r,t}^2 - 2y_{r,t}^2 + z_t^2)}{r^8} dx_r dy_r \quad (88)$$

$$\rho_{11}^{13} = k_0^2 \iint_{\mathcal{R}_r} \frac{-x_{r,t} z_t (x_{r,t}^2 + z_t^2)}{r^6} dx_r dy_r \quad (89)$$

$$\rho_{12}^{13} = \iint_{\mathcal{R}_r} \frac{x_{r,t} z_t (2y_{r,t}^2 - x_{r,t}^2 - z_t^2)}{r^8} dx_r dy_r \quad (90)$$

$$\rho_{11}^{23} = k_0^2 \iint_{\mathcal{R}_r} \frac{-y_{r,t} z_t (x_{r,t}^2 + z_t^2)}{r^6} dx_r dy_r \quad (91)$$

$$\rho_{12}^{23} = \iint_{\mathcal{R}_r} \frac{y_{r,t} z_t (2y_{r,t}^2 - x_{r,t}^2 - z_t^2)}{r^8} dx_r dy_r. \quad (92)$$

In the proof of Corollary 5, some first-order derivatives should be computed and the expressions are as follows.

$$\frac{\partial h(\mathbf{p}_r)}{\partial x_t} = x_{r,t} \left( j k_0 r^{-\frac{7}{2}} + \frac{5}{2} r^{-\frac{9}{2}} - \frac{r^{-\frac{5}{2}}}{f_{xz}} \right) f_{sz} \quad (93a)$$

$$\frac{\partial h(\mathbf{p}_r)}{\partial y_t} = y_{r,t} \left( \frac{5}{2} r^{-\frac{9}{2}} + j k_0 r^{-\frac{7}{2}} \right) f_{sz} \quad (93b)$$

$$\frac{\partial h(\mathbf{p}_r)}{\partial z_t} = \left( \frac{3z_t^2 + x_{r,t}^2}{2z_t f_{xz}} r^{-\frac{5}{2}} - j k_0 z_t r^{-\frac{7}{2}} - \frac{5}{2} z_t r^{-\frac{9}{2}} \right) f_{sz}. \quad (93c)$$

where  $f_{xz} = x_{r,t}^2 + z_t^2$  and  $f_{sz} = \sqrt{z_t f_{xz}} e^{-jk_0 r}$ .

The specific expressions of  $\rho_{21}^{mn}$  and  $\rho_{22}^{mn}$  are as follows.

$$\rho_{21}^{11} = k_0^2 z_t \iint_{\mathcal{R}_r} \frac{x_{r,t}^2 (x_{r,t}^2 + z_t^2)}{r^7} dx_r dy_r \quad (94)$$

$$\rho_{22}^{11} = z_t \iint_{\mathcal{R}_r} \frac{x_{r,t}^2 (25f_{xz}/4 - 5r^2 + f_{xz}^{-1} r^4)}{r^9} dx_r dy_r \quad (95)$$

$$\rho_{21}^{22} = k_0^2 z_t \iint_{\mathcal{R}_r} \frac{y_{r,t}^2 (x_{r,t}^2 + z_t^2)}{r^7} dx_r dy_r \quad (96)$$

$$\rho_{22}^{22} = z_t \iint_{\mathcal{R}_r} \frac{25y_{r,t}^2 (x_{r,t}^2 + z_t^2) / 4}{r^9} dx_r dy_r \quad (97)$$

$$\rho_{21}^{33} = k_0^2 z_t^3 \iint_{\mathcal{R}_r} \frac{x_{r,t}^2 + z_t^2}{r^7} dx_r dy_r \quad (98)$$

$$\rho_{22}^{33} = \iint_{\mathcal{R}_r} \frac{[x_{r,t}^2 (r^2 - 2z_t^2) + z_t^2 f_{yz}]^2}{4z_t (x_{r,t}^2 + z_t^2) r^9} dx_r dy_r \quad (99)$$

$$\rho_{21}^{12} = k_0^2 z_t \iint_{\mathcal{R}_r} \frac{x_{r,t} y_{r,t} (x_{r,t}^2 + z_t^2)}{r^7} dx_r dy_r \quad (100)$$

$$\rho_{22}^{12} = z_t \iint_{\mathcal{R}_r} \frac{x_{r,t} y_{r,t} (25f_{xz}/4 - 5r^2/2)}{r^9} dx_r dy_r \quad (101)$$

$$\rho_{21}^{13} = k_0^2 z_t^2 \iint_{\mathcal{R}_r} \frac{-x_{r,t} (x_{r,t}^2 + z_t^2)}{r^7} dx_r dy_r \quad (102)$$

$$\rho_{22}^{13} = \iint_{\mathcal{R}_r} \frac{x_{r,t} (f_{5z} f_{xz} - f_{3z} - 25z_t^2 f_{xz}^2 / 2)}{2 (x_{r,t}^2 + z_t^2) r^9} dx_r dy_r \quad (103)$$

$$\rho_{21}^{23} = k_0^2 z_t^2 \iint_{\mathcal{R}_r} \frac{-y_{r,t} (x_{r,t}^2 + z_t^2)}{r^7} dx_r dy_r \quad (104)$$

$$\rho_{22}^{23} = \iint_{\mathcal{R}_r} \frac{5y_{r,t} (f_{3z}/r^2 - 5z_t^2 f_{xz})}{4r^9} dx_r dy_r, \quad (105)$$

where  $f_{3z} = (x_{r,t}^2 + 3z_t^2) r^4$ ,  $f_{5z} = 5 (x_{r,t}^2 + 5z_t^2) r^2/2$ , and  $f_{yz} = 3y_{r,t}^2 - 2z_t^2$ .

In Corollary 6,  $\text{CRB}_3(\kappa_t)$  can be computed by (20) – (22) and  $I_{mn} = \rho_3^{mn}$ . The expressions of  $\rho_3^{mn}$  are as follows.

$$\rho_3^{11} = \frac{D^2}{2\alpha^2} \left| \sum_{i=1}^{\sqrt{\alpha}} \sum_{j=1}^{\sqrt{\alpha}} x_{i,t} g_{zx} \left( g_r - \frac{z_t}{|g_{zx}|^2} r_{i,j}^{-\frac{5}{2}} \right) \right|^2 \quad (106)$$

$$\rho_3^{22} = \frac{D^2}{2\alpha^2} \left| \sum_{i=1}^{\sqrt{\alpha}} \sum_{j=1}^{\sqrt{\alpha}} y_{j,t} g_{zx} g_r \right|^2 \quad (107)$$

$$\rho_3^{33} = \frac{D^2}{2\alpha^2} \left| \sum_{i=1}^{\sqrt{\alpha}} \sum_{j=1}^{\sqrt{\alpha}} g_{zx} \left( \frac{3z_t^2 + x_{i,t}^2}{2|g_{zx}|^2} r_{i,j}^{-\frac{5}{2}} - z_t g_r \right) \right|^2 \quad (108)$$

$$\rho_3^{12} = \frac{D^2}{2\alpha^2} \text{Re} \left\{ \left( \sum_{i=1}^{\sqrt{\alpha}} \sum_{j=1}^{\sqrt{\alpha}} y_{j,t} g_{zx} g_r \right) \cdot \left[ \sum_{i=1}^{\sqrt{\alpha}} \sum_{j=1}^{\sqrt{\alpha}} x_{i,t} g_{zx} \left( g_r - \frac{z_t}{|g_{zx}|^2} r_{i,j}^{-\frac{5}{2}} \right) \right]^* \right\} \quad (109)$$

$$\rho_3^{13} = \frac{D^2}{2\alpha^2} \text{Re} \left\{ \left[ \sum_{i=1}^{\sqrt{\alpha}} \sum_{j=1}^{\sqrt{\alpha}} g_{zx} \left( \frac{3z_t^2 + x_{i,t}^2}{2|g_{zx}|^2} r_{i,j}^{-\frac{5}{2}} - z_t g_r \right) \right] \cdot \left[ \sum_{i=1}^{\sqrt{\alpha}} \sum_{j=1}^{\sqrt{\alpha}} x_{i,t} g_{zx} \left( g_r - \frac{z_t}{|g_{zx}|^2} r_{i,j}^{-\frac{5}{2}} \right) \right]^* \right\} \quad (110)$$

$$\rho_3^{23} = \frac{D^2}{2\alpha^2} \text{Re} \left\{ \left[ \sum_{i=1}^{\sqrt{\alpha}} \sum_{j=1}^{\sqrt{\alpha}} g_{zx} \left( \frac{3z_t^2 + x_{i,t}^2}{2|g_{zx}|^2} r_{i,j}^{-\frac{5}{2}} - z_t g_r \right) \right] \cdot \left( \sum_{i=1}^{\sqrt{\alpha}} \sum_{j=1}^{\sqrt{\alpha}} y_{j,t} g_{zx} g_r \right)^* \right\}, \quad (111)$$

where  $x_{i,t} = x_i - x_t$ ,  $y_{j,t} = y_j - y_t$ ,  $g_r = \frac{5}{2} r_{i,j}^{-\frac{9}{2}} + j k_0 r_{i,j}^{-\frac{7}{2}}$ , and  $g_{zx} = \sqrt{z_t (z_t^2 + x_{i,t}^2)} e^{-jk_0 r_{i,j}}$ .

## APPENDIX C THE CLOSED-FORM EXPRESSIONS

The double integral formulas (28), (30), (31) and (32) can be computed in the following closed-form expressions.

$$\rho_{12x} = \frac{1}{\tau^2 + 8} \left[ \frac{f_t}{2\sqrt{\tau^2 + 8}} - \frac{\tau^2(3\tau^2 + 16)}{(\tau^2 + 4)^2} \right] \quad (112)$$

$$\rho_{12y} = \frac{(9\tau^4 + 152\tau^2 + 544)}{2(\tau^2 + 8)^{5/2} \tau^{-1} f_t^{-1}} + \frac{\tau^2(3\tau^4 + 8\tau^2 - 32)}{(\tau^2 + 8)^2 (\tau^2 + 4)^2} \quad (113)$$

$$\rho_{11z} = \frac{\tau}{\tau^2 + 8} \left[ \frac{(3\tau^2 + 28)}{\sqrt{\tau^2 + 8}} f_t + \frac{2\tau}{\tau^2 + 4} \right] \quad (114)$$

$$\rho_{12z} = \frac{2\tau}{(\tau^2 + 8)^2} \left[ \frac{\tau^4 + 16\tau^2 + 88}{\sqrt{\tau^2 + 8} f_t^{-1}} + \frac{16\tau(\tau^2 + 5)}{(\tau^2 + 4)^2} \right], \quad (115)$$

where  $f_t = \arctan \frac{\tau}{\sqrt{\tau^2 + 8}}$ .

To provide the closed-form upper and lower bounds of  $\rho_{11x}$  and  $\rho_{11y}$ , we denote two circular domains  $\mathcal{C}^- = \{(u, v) : u^2 + v^2 \leq (\frac{\tau}{\sqrt{8}})^2\}$ ,  $\mathcal{C}^+ = \{(u, v) : u^2 + v^2 \leq (\frac{\tau}{2})^2\}$  and two non-negative function  $g_{11x} = u^2(u^2 + 1)/(u^2 + v^2 + 1)^3$ ,  $g_{11y} = v^2(u^2 + 1)/(u^2 + v^2 + 1)^3$ , then we have

$$\iint_{\mathcal{C}^-} g_{11x} dudv < \rho_{11x} < \iint_{\mathcal{C}^+} g_{11x} dudv \quad (116)$$

$$\iint_{\mathcal{C}^-} g_{11y} dudv < \rho_{11y} < \iint_{\mathcal{C}^+} g_{11y} dudv. \quad (117)$$

Therefore, the closed-form upper and lower bounds of (27) and (29) can be derived as follows.

$$\iint_{\mathcal{C}^+} g_{11x} dudv = \frac{3\pi}{8} \ln \left( 1 + \frac{\tau^2}{4} \right) - \frac{\pi\tau^2(5\tau^2 + 24)}{16(\tau^2 + 4)^2} \quad (118)$$

$$\iint_{\mathcal{C}^-} g_{11x} dudv = \frac{3\pi}{8} \ln \left( 1 + \frac{\tau^2}{8} \right) - \frac{\pi\tau^2(5\tau^2 + 48)}{16(\tau^2 + 8)^2} \quad (119)$$

$$\iint_{\mathcal{C}^+} g_{11y} dudv = \frac{\pi}{8} \ln \left( 1 + \frac{\tau^2}{4} \right) + \frac{\pi\tau^2(\tau^2 - 8)}{16(\tau^2 + 4)^2} \quad (120)$$

$$\iint_{\mathcal{C}^-} g_{11y} dudv = \frac{\pi}{8} \ln \left( 1 + \frac{\tau^2}{8} \right) + \frac{\pi\tau^2(\tau^2 - 16)}{16(\tau^2 + 8)^2}. \quad (121)$$

Similarly, we denote  $g_{2i\kappa}$ ,  $i = 1, 2$  as the integrand functions of (35) – (40), then we have

$$\rho_{2i\kappa}^{(l)} = \iint_{\mathcal{C}^-} g_{2i\kappa} dudv < \rho_{2i\kappa} < \iint_{\mathcal{C}^+} g_{2i\kappa} dudv = \rho_{2i\kappa}^{(u)}. \quad (122)$$

The closed-form upper and lower bounds of  $\rho_{21\kappa}$  and  $\rho_{22\kappa}$  can be computed as follows.

$$\rho_{21x}^{(u)} = \frac{8\pi}{15} - \frac{\pi(45\tau^4 + 320\tau^2 + 512)}{30(\tau^2 + 4)^{5/2}} \quad (123)$$

$$\rho_{21x}^{(l)} = \frac{8\pi}{15} - \frac{\sqrt{2}\pi(45\tau^4 + 640\tau^2 + 2048)}{30(\tau^2 + 8)^{5/2}} \quad (124)$$

$$\rho_{22x}^{(u)} = \frac{3\pi}{14} - \frac{\pi(63\tau^4 - 112\tau^2\sqrt{\tau^2 + 4})}{14(\tau^2 + 4)^{7/2}} - \frac{\pi(672\tau^2 - 448\sqrt{\tau^2 + 4} + 1280)}{14(\tau^2 + 4)^{7/2}} \quad (125)$$

$$\rho_{22x}^{(l)} = \frac{3\pi}{14} - \frac{\pi(63\sqrt{2}\tau^4 + 1344\sqrt{2}\tau^2)}{7(\tau^2 + 8)^{7/2}} + \frac{\pi[224(\tau^2 + 8)^{3/2} - 5120\sqrt{2}]}{7(\tau^2 + 8)^{7/2}} \quad (126)$$

$$\rho_{21y}^{(u)} = \frac{4\pi}{15} - \frac{\pi(15\tau^4 + 160\tau^2 + 256)}{30(\tau^2 + 4)^{5/2}} \quad (127)$$

$$\rho_{21y}^{(l)} = \frac{4\pi}{15} - \frac{\sqrt{2}\pi(15\tau^4 + 320\tau^2 + 1024)}{30(\tau^2 + 8)^{5/2}} \quad (128)$$

$$\rho_{22y}^{(u)} = \frac{10\pi}{21} - \frac{5\pi(35\tau^4 + 448\tau^2 + 512)}{42(\tau^2 + 4)^{7/2}} \quad (129)$$

$$\rho_{22y}^{(l)} = \frac{10\pi}{21} - \frac{5\sqrt{2}\pi(35\tau^4 + 896\tau^2 + 2048)}{21(\tau^2 + 8)^{7/2}} \quad (130)$$

$$\rho_{21z}^{(u)} = \frac{8\pi}{15} - \frac{8\pi(5\tau^2 + 32)}{15(\tau^2 + 4)^{5/2}} \quad (131)$$

$$\rho_{21z}^{(l)} = \frac{8\pi}{15} \left[ 1 - \frac{10\sqrt{2}}{(\tau^2 + 8)^{3/2}} - \frac{48\sqrt{2}}{(\tau^2 + 8)^{5/2}} \right] \quad (132)$$

$$\rho_{22z}^{(u)} = \frac{13\pi}{42} - \frac{\pi(21\tau^6 + 224\tau^4 - 896\tau^2)}{42(\tau^2 + 4)^{7/2}} + \frac{512\pi}{21(\tau^2 + 4)^{7/2}} - \frac{\pi(168\tau^2 + 672)}{21(\tau^2 + 4)^3} \quad (133)$$

$$\rho_{22z}^{(l)} = \frac{13\pi}{42} - \frac{\pi(21\sqrt{2}\tau^6 + 448\sqrt{2}\tau^4)}{42(\tau^2 + 8)^{7/2}} - \frac{\pi[1344(\tau^2 + 8)^{3/2} - \sqrt{2}]}{42(\tau^2 + 8)^{7/2}}. \quad (134)$$

#### APPENDIX D PROOF OF COROLLARY 10

We only need to prove that  $k_0^2 \rho_{11\kappa} \gg z_t^2 \rho_{12\kappa}$  and  $k_0^2 \rho_{21\kappa} \gg z_t^2 \rho_{22\kappa}$  for  $z_t \gg \lambda$ , then the approximation in Corollary 10 can be proved immediately.

When  $z_t \gg \lambda$ , we have  $k_0^2 \gg z_t^{-2}$ . Observe that

$$2\rho_{11x} > \iint_{\mathcal{R}_\tau} \frac{2u^2(u^2 + 1)}{(u^2 + v^2 + 1)^4} dudv > \rho_{12x} > 0, \quad (135)$$

from which we obtain

$$k_0^2 \rho_{11x} \gg z_t^{-2} \rho_{12x}. \quad (136)$$

Similarly, we have

$$\frac{u^2 + 1}{(u^2 + v^2 + 1)^3} \geq \frac{v^4 + u^2 v^2 + 1}{(u^2 + v^2 + 1)^4} > 0. \quad (137)$$

Then, we have that  $\rho_{11z} > \rho_{12z}$ . Accordingly, we have that

$$k_0^2 \rho_{11z} \gg z_t^{-2} \rho_{12z}. \quad (138)$$

Observe that

$$4\pi^2 \rho_{21y} > \iint_{\mathcal{R}_\tau} \frac{4\pi^2 v^2 (u^2 + 1)}{(u^2 + v^2 + 1)^{9/2}} dudv > \rho_{22y} > 0. \quad (139)$$

So the following inequality can be proved.

$$k_0^2 \rho_{21y} \gg z_t^{-2} \rho_{22y}. \quad (140)$$

Note that the remaining inequalities are challenging to demonstrate analytically, therefore we provide numerical proofs. If we define the difference function  $f_{dy1}(\tau) = \rho_{11y} - \rho_{12y}$ , we can deduce from (113) and (121) that the minimum value of the function  $f_{dy1}(\tau)$  is greater than  $-2.34$ , which testifies that

$$k_0^2 \rho_{11y} \gg z_t^{-2} \rho_{12y}. \quad (141)$$

Define the difference function  $f_{dx2}(\tau) = \rho_{21x} - \rho_{22x}$ , from (124) and (125), we have that  $f_{dx2}(\tau) > \rho_{21x}^{(l)} - \rho_{22x}^{(u)}$ , and we can derive that the minimum value of the function  $f_{dx2}(\tau)$  is greater than  $67\pi/210 - 1.23 \approx -0.23$ , which indicates that

$$k_0^2 \rho_{21x} \gg z_t^{-2} \rho_{21x}. \quad (142)$$

Similarly, we define the difference function  $f_{dz2}(\tau) = \rho_{21z} - \rho_{22z}$ , then we have that  $f_{dz2}(\tau) > \rho_{21z}^{(l)} - \rho_{22z}^{(u)}$  based on (132) and (133). Next, we can deduce that the minimum value of the function  $f_{dz2}(\tau)$  is greater than  $47\pi/210 - 0.80 \approx -0.10$ , which verifies that

$$k_0^2 \rho_{21z} \gg z_t^{-2} \rho_{22z}. \quad (143)$$

Therefore, Corollary 10 holds.

#### REFERENCES

- [1] G. Bresson, Z. Alsayed, L. Yu, and S. Glaser, "Simultaneous localization and mapping: A survey of current trends in autonomous driving," *IEEE Transactions on Intelligent Vehicles*, vol. 2, no. 3, pp. 194–220, 2017.
- [2] K. Witrals, P. Meissner, E. Leitinger, Y. Shen, C. Gustafson, F. Tufvesson, K. Haneda, D. Dardari, A. F. Molisch, A. Conti, and M. Z. Win, "High-accuracy localization for assisted living: 5g systems will turn multipath channels from foe to friend," *IEEE Signal Processing Magazine*, vol. 33, no. 2, pp. 59–70, 2016.
- [3] F. Meyer, B. Etxlinger, Z. Liu, F. Hlawatsch, and M. Z. Win, "A scalable algorithm for network localization and synchronization," *IEEE Internet of Things Journal*, vol. 5, no. 6, pp. 4714–4727, 2018.
- [4] X. Chen, Z. Feng, Z. Wei, F. Gao, and X. Yuan, "Performance of joint sensing-communication cooperative sensing uav network," *IEEE Transactions on Vehicular Technology*, vol. 69, no. 12, pp. 15 545–15 556, 2020.
- [5] A. Liu, Z. Huang, M. Li, Y. Wan, W. Li, T. X. Han, C. Liu, R. Du, D. K. P. Tan, J. Lu *et al.*, "A survey on fundamental limits of integrated sensing and communication," *IEEE Communications Surveys & Tutorials*, 2022.
- [6] M. Z. Win, Y. Shen, and W. Dai, "A theoretical foundation of network localization and navigation," *Proceedings of the IEEE*, vol. 106, no. 7, pp. 1136–1165, 2018.
- [7] J. A. del Peral-Rosado, R. Raulefs, J. A. López-Salcedo, and G. Seco-Granados, "Survey of cellular mobile radio localization methods: From 1g to 5g," *IEEE Communications Surveys & Tutorials*, vol. 20, no. 2, pp. 1124–1148, 2017.
- [8] D. Dardari, P. Closas, and P. M. Djurić, "Indoor tracking: Theory, methods, and technologies," *IEEE Transactions on Vehicular Technology*, vol. 64, no. 4, pp. 1263–1278, 2015.
- [9] M. Z. Win, A. Conti, S. Mazuelas, Y. Shen, W. M. Gifford, D. Dardari, and M. Chiani, "Network localization and navigation via cooperation," *IEEE Communications Magazine*, vol. 49, no. 5, pp. 56–62, 2011.
- [10] A. Shahmansoori, G. E. Garcia, G. Destino, G. Seco-Granados, and H. Wymeersch, "Position and orientation estimation through millimeter-wave mimo in 5g systems," *IEEE Transactions on Wireless Communications*, vol. 17, no. 3, pp. 1822–1835, 2018.
- [11] Y. Han, Y. Shen, X.-P. Zhang, M. Z. Win, and H. Meng, "Performance limits and geometric properties of array localization," *IEEE Transactions on Information Theory*, vol. 62, no. 2, pp. 1054–1075, 2015.
- [12] A. Guerra, F. Guidi, and D. Dardari, "Single-anchor localization and orientation performance limits using massive arrays: MIMO vs. beamforming," *IEEE Transactions on Wireless Communications*, vol. 17, no. 8, pp. 5241–5255, 2018.
- [13] J. Sherman, "Properties of focused apertures in the fresnel region," *IRE Transactions on Antennas and Propagation*, vol. 10, no. 4, pp. 399–408, 1962.
- [14] E. G. Larsson, O. Edfors, F. Tufvesson, and T. L. Marzetta, "Massive mimo for next generation wireless systems," *IEEE communications magazine*, vol. 52, no. 2, pp. 186–195, 2014.
- [15] L. Lu, G. Y. Li, A. L. Swindlehurst, A. Ashikhmin, and R. Zhang, "An overview of massive mimo: Benefits and challenges," *IEEE journal of selected topics in signal processing*, vol. 8, no. 5, pp. 742–758, 2014.

- [16] E. Björnson, L. Sanguinetti, H. Wymeersch, J. Hoydis, and T. L. Marzetta, "Massive mimo is a reality—what is next?: Five promising research directions for antenna arrays," *Digital Signal Processing*, vol. 94, pp. 3–20, 2019.
- [17] W. Tang, M. Z. Chen, J. Y. Dai, Y. Zeng, X. Zhao, S. Jin, Q. Cheng, and T. J. Cui, "Wireless communications with programmable metasurface: New paradigms, opportunities, and challenges on transceiver design," *IEEE Wireless Communications*, vol. 27, no. 2, pp. 180–187, 2020.
- [18] A. Ghosh, T. A. Thomas, M. C. Cudak, R. Ratasuk, P. Moorut, F. W. Vook, T. S. Rappaport, G. R. MacCartney, S. Sun, and S. Nie, "Millimeter-wave enhanced local area systems: A high-data-rate approach for future wireless networks," *IEEE Journal on Selected Areas in Communications*, vol. 32, no. 6, pp. 1152–1163, 2014.
- [19] T. S. Rappaport, Y. Xing, O. Kanhere, S. Ju, A. Madanayake, S. Mandal, A. Alkhatieb, and G. C. Trichopoulos, "Wireless communications and applications above 100 ghz: Opportunities and challenges for 6g and beyond," *IEEE access*, vol. 7, pp. 78 729–78 757, 2019.
- [20] I. F. Akyildiz, C. Han, and S. Nie, "Combating the distance problem in the millimeter wave and terahertz frequency bands," *IEEE Communications Magazine*, vol. 56, no. 6, pp. 102–108, 2018.
- [21] K. T. Selvan and R. Janaswamy, "Fraunhofer and fresnel distances: Unified derivation for aperture antennas," *IEEE Antennas and Propagation Magazine*, vol. 59, no. 4, pp. 12–15, 2017.
- [22] M. Cui, Z. Wu, Y. Lu, X. Wei, and L. Dai, "Near-field communications for 6g: Fundamentals, challenges, potentials, and future directions," *arXiv preprint arXiv:2203.16318*, 2022.
- [23] H. Zhang, N. Shlezinger, F. Guidi, D. Dardari, M. F. Imani, and Y. C. Eldar, "Beam focusing for near-field multi-user mimo communications," *IEEE Transactions on Wireless Communications*, 2022.
- [24] Y. Rockah and P. Schultheiss, "Array shape calibration using sources in unknown locations—part ii: Near-field sources and estimator implementation," *IEEE Transactions on Acoustics, Speech, and Signal Processing*, vol. 35, no. 6, pp. 724–735, 1987.
- [25] E. Grosicki, K. Abed-Meraim, and Y. Hua, "A weighted linear prediction method for near-field source localization," *IEEE Transactions on Signal Processing*, vol. 53, no. 10, pp. 3651–3660, 2005.
- [26] J.-F. Chen, X.-L. Zhu, and X.-D. Zhang, "A new algorithm for joint range-doa-frequency estimation of near-field sources," *EURASIP Journal on Advances in Signal Processing*, vol. 2004, no. 3, pp. 1–7, 2004.
- [27] K. Deng, Q. Yin, and H. Wang, "Closed form parameters estimation for near field sources," in *2007 IEEE International Symposium on Circuits and Systems*. IEEE, 2007, pp. 3251–3254.
- [28] Y.-S. Hsu, K. T. Wong, and L. Yeh, "Mismatch of near-field bearing-range spatial geometry in source-localization by a uniform linear array," *IEEE transactions on antennas and propagation*, vol. 59, no. 10, pp. 3658–3667, 2011.
- [29] K. Haneda, J.-i. Takada, and T. Kobayashi, "A parametric uwb propagation channel estimation and its performance validation in an anechoic chamber," *IEEE Transactions on Microwave Theory and Techniques*, vol. 54, no. 4, pp. 1802–1811, 2006.
- [30] X. Yin, S. Wang, N. Zhang, and B. Ai, "Scatterer localization using large-scale antenna arrays based on a spherical wave-front parametric model," *IEEE Transactions on Wireless Communications*, vol. 16, no. 10, pp. 6543–6556, 2017.
- [31] F. Guidi and D. Dardari, "Radio positioning with em processing of the spherical wavefront," *IEEE Transactions on Wireless Communications*, vol. 20, no. 6, pp. 3571–3586, 2021.
- [32] Y.-D. Huang and M. Barkat, "Near-field multiple source localization by passive sensor array," *IEEE Transactions on antennas and propagation*, vol. 39, no. 7, pp. 968–975, 1991.
- [33] N. Yuen and B. Friedlander, "Performance analysis of higher order esprit for localization of near-field sources," *IEEE Transactions on Signal Processing*, vol. 46, no. 3, pp. 709–719, 1998.
- [34] W. Zhi and M. Y.-W. Chia, "Near-field source localization via symmetric subarrays," in *2007 IEEE International Conference on Acoustics, Speech and Signal Processing - ICASSP '07*, vol. 2, 2007, pp. II–1121–II–1124.
- [35] J. Liang and D. Liu, "Passive localization of mixed near-field and far-field sources using two-stage music algorithm," *IEEE Transactions on Signal Processing*, vol. 58, no. 1, pp. 108–120, 2009.
- [36] W. Zuo, J. Xin, N. Zheng, and A. Sano, "Subspace-based localization of far-field and near-field signals without eigendecomposition," *IEEE Transactions on Signal Processing*, vol. 66, no. 17, pp. 4461–4476, 2018.
- [37] S. Zhang, T. Jost, R. Pöhlmann, A. Dammann, D. Shutin, and P. A. Hoehner, "Spherical wave positioning based on curvature of arrival by an antenna array," *IEEE Wireless Communications Letters*, vol. 8, no. 2, pp. 504–507, 2019.
- [38] J. Yang, Y. Zeng, S. Jin, C.-K. Wen, and P. Xu, "Communication and localization with extremely large lens antenna array," *IEEE Transactions on Wireless Communications*, vol. 20, no. 5, pp. 3031–3048, 2021.
- [39] H. Gazzah and J. P. Delmas, "Crb-based design of linear antenna arrays for near-field source localization," *IEEE Transactions on Antennas and Propagation*, vol. 62, no. 4, pp. 1965–1974, 2014.
- [40] H. Wymeersch, "A fisher information analysis of joint localization and synchronization in near field," in *2020 IEEE International Conference on Communications Workshops (ICC Workshops)*, 2020, pp. 1–6.
- [41] J. P. Delmas, M. N. El Korso, H. Gazzah, and M. Castella, "Crb analysis of planar antenna arrays for optimizing near-field source localization," *Signal Processing*, vol. 127, pp. 117–134, 2016.
- [42] B. Friedlander, "Localization of signals in the near-field of an antenna array," *IEEE Transactions on Signal Processing*, vol. 67, no. 15, pp. 3885–3893, 2019.
- [43] A. de Jesus Torres, A. A. D'Amico, L. Sanguinetti, and M. Z. Win, "Cramér-rao bounds for near-field localization," in *2021 55th Asilomar Conference on Signals, Systems, and Computers*. IEEE, 2021, pp. 1250–1254.
- [44] C. Huang, S. Hu, G. C. Alexandropoulos, A. Zappone, C. Yuen, R. Zhang, M. Di Renzo, and M. Debbah, "Holographic mimo surfaces for 6g wireless networks: Opportunities, challenges, and trends," *IEEE Wireless Communications*, vol. 27, no. 5, pp. 118–125, 2020.
- [45] D. Dardari and N. Decarli, "Holographic communication using intelligent surfaces," *IEEE Communications Magazine*, vol. 59, no. 6, pp. 35–41, 2021.
- [46] A. Pizzo, T. L. Marzetta, and L. Sanguinetti, "Spatially-stationary model for holographic mimo small-scale fading," *IEEE Journal on Selected Areas in Communications*, vol. 38, no. 9, pp. 1964–1979, 2020.
- [47] S. Hu, F. Rusek, and O. Edfors, "Beyond massive mimo: The potential of data transmission with large intelligent surfaces," *IEEE Transactions on Signal Processing*, vol. 66, no. 10, pp. 2746–2758, 2018.
- [48] —, "Beyond massive mimo: The potential of positioning with large intelligent surfaces," *IEEE Transactions on Signal Processing*, vol. 66, no. 7, pp. 1761–1774, 2018.
- [49] D. Dardari, "Communicating with large intelligent surfaces: Fundamental limits and models," *IEEE Journal on Selected Areas in Communications*, vol. 38, no. 11, pp. 2526–2537, 2020.
- [50] E. Björnson, Ö. T. Demir, and L. Sanguinetti, "A primer on near-field beamforming for arrays and reconfigurable intelligent surfaces," *arXiv preprint arXiv:2110.06661*, 2021.
- [51] S. M. Kay, *Fundamentals of statistical signal processing: estimation theory*. Prentice-Hall, Inc., 1993.
- [52] A. S. Poon, R. W. Brodersen, and D. N. Tse, "Degrees of freedom in multiple-antenna channels: A signal space approach," *IEEE Transactions on Information Theory*, vol. 51, no. 2, pp. 523–536, 2005.
- [53] R. F. Harrington, *Time-harmonic electromagnetic fields*. McGraw-Hill College, 1961.